Journal of
Composites Science

MDPI

Article

Phase Field Modelling of Failure in Thermoset Composites Under Cure-Induced Residual Stress

Aravind Balaji [1,2,*], David Dumas [1] and Olivier Pierard [1]

[1] Cenaero Research Center, Rue des Frères Wright 29, 6041 Charleroi, Belgium; david.dumas@cenaero.be (D.D.)
[2] Department of Mechanical Engineering, Politecnico di Milano, via La Masa 1, 20156 Milan, Italy
* Correspondence: aravind.balaji@cenaero.be; Tel.: +32-497-62-62-79

Abstract: This study examines the residual stress induced by manufacturing and its effect on failure in thermosetting unidirectional composites under quasi-static loading, using Finite Element-based computational models. During the curing process, the composite material develops residual stress fields due to various phenomena. These stress fields are predicted using a constitutive viscoelastic model and subsequently initialized within a damage-driven Phase Field model. Structural tensors are used to modify the stress-based failure criteria to account for inherent transverse isotropy. This influence is incorporated into the crack phase field evolution equation, enabling a modular framework that retains all residual stress information through a heat-transfer analogy. The proposed coupled computational model is validated through a representative numerical case study involving L-shaped composite parts. The findings reveal that cure-induced residual stresses, in conjunction with discontinuities, play a critical role in matrix cracking and significantly affect the structural load-carrying capacity. The proposed coupled numerical approach provides an initial estimation of the influence of manufacturing defects and streamlines the optimization of cure profiles to enhance manufacturing quality. Among the investigated curing strategies, the three-dwell cure cycle emerged as the most effective solution.

Keywords: virtual manufacturing; residual stress; phase field; damage

Citation: Balaji, A.; Dumas, D.; Pierard, O. Phase Field Modelling of Failure in Thermoset Composites Under Cure-Induced Residual Stress. *J. Compos. Sci.* **2024**, *8*, 533. https://doi.org/10.3390/jcs8120533

Academic Editor: Zhong Hu

Received: 25 October 2024
Revised: 4 December 2024
Accepted: 11 December 2024
Published: 15 December 2024

1. Introduction

Thermosetting composite materials are extensively utilized in the aerospace industry because of their exceptional stiffness and outstanding in-plane strength-to-weight ratio [1]. Research in the previous decades has shown that several iterative analyses, such as the selection and optimization of composite materials (resin and fiber), mold characteristics, and other factors, are required to develop an effective manufacturing process [1,2]. This is mainly caused by manufacturing defects that occur during the manufacturing process [3,4]. Additionally, during manufacturing, composite parts attain residual stresses while being processed in the mold, even in the absence of external forces or thermal gradients, as noted in [5]. The final shape of the manufactured part deviates from the desirable design due to the uneven distribution of residual stresses during manufacturing. These residual stresses not only cause deformation, but also remain partially embedded within the parts after the process. This "locked-in" residual stress significantly affects damage and failure propagation, particularly interlaminar delamination and intralaminar matrix cracking [6–8]. Therefore, it is vital to develop methods that can accurately predict the effect of internal residual stress fields on the structural behavior of thermoset parts under different manufacturing conditions.

The formation of internal residual stresses is attributed to various factors that range from micro- to macro-scales. Residual stresses in fiber-reinforced polymer–matrix thermoset composites are largely inevitable due to the differing properties of the fiber and resin throughout the curing process [9,10], also known as the polymerization reaction. During

this phase, the thermosetting resin transitions from a viscous to a rubbery, and then finally, a glassy state. This results in the development of internal residual stresses and deformations related to the material's chemical and thermal behavior [11–13]. Chemical shrinkage, associated with the Coefficients of Chemical Shrinkage (CCS), occurs as the resin undergoes curing, leading to a reduction in its free volume. As the temperature rises, the resin molecules undergo end-linking reactions that draw them inwards, resulting in transitions between different states. Consequently, the available space within the resin decreases, exerting pressure on the fibers and generating internal residual stress that is uniformly distributed throughout the composite laminate. Additionally, thermally induced stress fields arise from the mismatch between the Coefficients of Thermal Expansion (CTE) of the resin and the fibers. A diverse set of approaches is being employed to evaluate internal residual stress in thermosetting composites [14]. Upon demolding, the majority of these stresses are released, causing the manufactured thermoset parts to assume distorted shapes. It is also important to acknowledge that factors such as the part thickness, curing boundary conditions, mold material, and lay-up configuration significantly affect the final residual stress field [15–18].

The need to include internal residual stress fields alongside deformation predictions for a more comprehensive failure analysis through structural simulations highlights the significance of constitutive models. In recent decades, Finite Element Analysis (FEA) coupled with constitutive models has demonstrated a high effectiveness in predicting residual stresses [19]. Fully viscoelastic models [20–23] accurately depict curing behavior but require extensive material characterization and involve high computational costs [5]. Meanwhile, the Cure Hardening Instantaneously Linear Elastic (CHILE) model establishes simpler elastic relations to describe changes in composite thermo-chemo-mechanical properties based on cure process variables, incorporating a viscoelastic model that accounts for the path dependence of these variables [24–26]. A classic example of the CHILE model is presented in a previous study [25], where a simplified viscoelastic model incorporating the path dependence on cure state variables is utilized. Upon the demolding step in the numerical analysis, the implications and nature of the possible residual stresses during manufacturing can be further explored to assess their impact on the structural response of the part.

Thermoset composite parts formed into different types of profiles are extensively used in aerospace structures as reinforcement and present possible failure modes including delamination and matrix cracks [27–31]. Studies on these subjects provide an insight into the interaction between inter- and intralaminar damage. In general, these phenomena exhibit distinct failure mechanisms, making damage and failure modeling a persistent challenge. Within the context of Finite Element (FE)-based tools at the meso-scale level, various approaches exist for predicting failure mechanisms [32]. These approaches are commonly categorized into discrete and smeared continuum models. Among the widely used approaches for predicting coupled failure interactions is the Cohesive Zone Model (CZM), which is well discussed in many numerical studies [27–29,33–36]. The CZM facilitates the modelling of crack initiation and progression through a traction-separation law. Although the CZM can be easily implemented within an FE framework, it is crucial to identify in advance the zones where delamination or matrix cracking is likely to occur. This identification can be quite cumbersome in the case of 3D problems. Additionally, the process may encounter convergence issues due to physical or numerical instability [37,38]. Even with approaches like the extended FE Method(X-FEM), challenges arise, such as the need for re-meshing and difficulties in explicitly representing and tracking crack paths, particularly in 3D problems involving multiple interacting inter- and intralaminar cracks [39].

In this study, we utilize the widely used smeared Phase Field (PF) model [40]. The variational PF model has gained significant attention from computational studies to predict the formation, growth, and failure of cracks within and between layers of composite parts. This approach employs a thermodynamic framework in which crack propagation occurs once the fracture toughness exceeds the material's critical toughness [41,42]. A scalar

variable is utilized to implement a diffuse region of finite width, which characterizes the discrete crack surface and, in turn, describes the material's damage [43,44]. This feature provides a diffuse representation of fracture surfaces, such as delamination and matrix cracks, allowing for a seamless transition from the undamaged material to the damaged region. By utilizing diffusive damage representation, the model effectively tracks crack growth without requiring any additional criteria, thereby simplifying the process of modeling crack progression [40]. Previous reviews provide a detailed analysis of PF modeling for failure in composites [45,46]. Recent advancements in the PF model have addressed the modeling aspects of delamination and anisotropic bulk fracture, as explored by many researchers [47–59]. For composites at the meso-scale, anisotropy is introduced by considering structural tensors in the crack surface density function. Structural tensors are employed to modify energetic and failure criteria to account for inherent anisotropies [49,60,61]. The adjusted failure criteria, incorporating structural tensors, impact the driving force, and this influence is integrated into the crack PF evolution equation, facilitating the establishment of a modular structure. The PF approach is favored for its simplicity and its ability to couple with cure-induced residual stresses at the lamina level. In the present study, a comprehensive 3D mixed-mode PF framework is implemented to numerically model the progressive failure process associated with delamination and matrix cracking, taking into account the "locked-in" residual stresses post-manufacturing.

Manufacturing defects, such as residual stress, voids, and pre-cracks, are omnipresent in composites and are inherently unavoidable. Despite recent advancements in numerical modeling [62–66], effectively modeling composite failure when defects like voids and residual stresses coexist at the lamina level remains insufficient. The existing literature indicates a significant gap in understanding 3D defect distribution and stress variation, both of which are critical for accurately determining failure characteristics. It is essential to investigate how such interactions jointly influence composite failure, especially under varying manufacturing conditions. Moreover, such analyses can help us understand mechanisms like the effects of thermal expansion, cure shrinkage, and part–mold interactions, which alter the residual stress and subsequently affect the structural response. Within this study, we investigate cure-induced residual stress and its impact on failure in unidirectional (UD) fiber-reinforced polymer–matrix composites subjected to quasi-static loading conditions. We utilize a coupled FE-based CHILE model, followed by a PF approach, which incorporates structural numerical analyses with initialized residual stresses. Unlike X-FEM, which loses residual stress data during remeshing, or CZM, which struggles with defining traction-separation laws and numerical stability, the coupled CHILE-PF approach remains efficient, requiring fewer calibration parameters. Moreover, the approach is simpler and more efficient for handling parts with discontinuities, such as voids. The effectiveness of the proposed coupled computational models is demonstrated through representative numerical examples, including L-shaped curved thermoset parts manufactured under the Manufacturing Recommended Curing Cycle (MRCC). Additionally, for thicker parts, we employ the concept of heat-transfer analogy to model the influence of stochastic voids on the load-carrying capacity. This coupled numerical approach to progressive damage offers an initial assessment of the impact of manufacturing defects and facilitates the optimization of cure temperature profiles.

2. Methods

In this section, we provide a detailed discussion of the computational methods corresponding to the CHILE model and the PF model used to simulate the manufacturing cure and structural simulations. Firstly, Section 2.1 addresses the modeling of cure-induced residual stresses arising from manufacturing processes. This is followed by a review of the PF model for rate-independent failures under quasi-static conditions, including considerations of residual stresses. This section also includes a discussion on the calibration of parameters related to the PF model and the selection of the degradation function, as applied

to UD composites at the meso-scale. Finally, we elaborate on the numerical implementation of the coupled computational models.

2.1. Cure Hardening Instantaneous Linear Elastic Constitutive (CHILE) Model

The commonly used computational approach for predicting the residual stress field involves FE-based tools with constitutive models. The classic CHILE model was proposed in [25], which exploits path dependence on cure state variables within the study. The instantaneous relaxation modulus of Maxwell's element, comprising a dashpot and spring system within the viscoelastic model of the partially cured resin, is influenced by the cure state variables, namely the degree of cure, ϱ, and the glass transition temperature, T_g. Appendix A provides detailed information on how the cure state variables influence the volumetric free strains, $\boldsymbol{\varepsilon}$. The viscoelastic model of the partially cured resin is influenced by the reduced time associated with the dashpot and spring, represented by Y' and Y, respectively. The thermo-viscoelastic behavior of the materials is described in integral form, incorporating the linear elastic Hooke tensor, $\boldsymbol{C}$. The equation is given as follows:

$$\boldsymbol{\sigma}(t) = \boldsymbol{C}\boldsymbol{\varepsilon} + \int_0^t \delta\boldsymbol{C}(Y - Y')\frac{\partial(\boldsymbol{\varepsilon}_{\text{mech}} - \boldsymbol{\varepsilon})}{\partial\urcorner}\,\partial\urcorner \tag{1}$$

where $\boldsymbol{\sigma}$ represents the stress, $\delta\boldsymbol{C}$ represents the independent relaxation function of N Maxwell elements, and $\boldsymbol{\varepsilon}_{\text{mech}}$ and $\boldsymbol{\varepsilon}$ denote the mechanical non-volumetric free strain and volumetric free strain, respectively. The dependence of Y and Y' on state variables is defined through a shift factor, a_T, given by

$$Y = \int_0^t \frac{1}{a_T}dt'\,; Y' = \int_0^{\urcorner} \frac{1}{a_T}d\urcorner' \tag{2}$$

The Maxwell's model with N elements, assembled in parallel with a free spring, provides $\boldsymbol{C}$ as follows:

$$\boldsymbol{C} = \begin{cases} 0,\ \forall\ \varrho < \varrho_{\text{gel}} \\ \boldsymbol{C}_\infty + \sum\limits_{n=1}^{N} \boldsymbol{C}_n\, e^{((-t)\rho^n)}\ ,\forall\ \varrho\ \geq\ \varrho_{\text{gel}} \end{cases} \tag{3}$$

where $\boldsymbol{C}_\infty$ represents the fully relaxed modulus of uncured resin, $\boldsymbol{C}_n$ denotes the spring constant, ρ^n are the relaxation times, with n indicating the number of Maxwell elements. The variable ϱ_{gel} refers to the degree of cure at which the material transitions to the rubbery state. The shift factor, a_T, is assumed to tend toward infinity in the glassy state and approaches zero in the rubbery state. Additionally, a variable, ι, is incorporated to establish the mathematical approximation of a_T, as expressed by

$$a_T = \lim_{\gamma\to 0}\begin{cases} \iota, \forall\ T\ \geq\ T_g(\varrho) \\ \frac{1}{\iota}\ ,\ \forall\ T <\ T_g(\varrho) \end{cases} \tag{4}$$

where T denotes the part temperature. This assumption dictates the Hooke tensor: in the rubbery state, $\boldsymbol{C}_r$ is referred as the fully relaxed Hooke tensor, $\boldsymbol{C}_\infty$, while in the glassy state, $\boldsymbol{C}_g$ is expressed as $(\boldsymbol{C}_\infty + \sum_{n=1}^{N}\boldsymbol{C}_n)$. The stress increment, $\Delta\boldsymbol{\sigma}$, is given by

$$\Delta\boldsymbol{\sigma} = \left(\boldsymbol{C}_\infty + \frac{1}{\Delta Y}\sum_{n=1}^{N}\rho^n\boldsymbol{C}_n\, e^{\left(\frac{-\Delta Y}{\rho^n}\right)}\right)(\boldsymbol{\varepsilon}_{\text{mech}} - \boldsymbol{\varepsilon}) - \sum_{n=1}^{N}\left(1 - e^{\left(\frac{-\Delta Y}{\rho^n}\right)}\right)\boldsymbol{\sigma}^n_{\text{res}}(t) \tag{5}$$

where $\boldsymbol{\sigma}_{\text{res}}$ represents the locked-in residual stress field, initially set to 0, which is determined using a recursive update:

$$\boldsymbol{\sigma}_{\text{res}}(t + \Delta t) = \left(1 - e^{\left(\frac{-\Delta Y}{\rho^n}\right)}\right)\boldsymbol{\sigma}^n_{\text{res}}(t) + \rho^n\frac{\Delta(\boldsymbol{\varepsilon}_{\text{mech}} - \boldsymbol{\varepsilon})}{\Delta Y}\boldsymbol{C}_n\left(e^{\left(\frac{-\Delta Y}{\rho^n}\right)}\right) \tag{6}$$

This is integrated into the FE tool using the method in [67]. The reduced time is expressed as $\Delta Y = \Delta t / a_T$. An incremental formulation is developed by substituting the rate dependence with a path dependence on the curing process variables, following Equations (1)–(4). The stress increment, when simplified, corresponds to Δt, and is expressed as

$$\Delta\boldsymbol{\sigma} = \begin{cases} \boldsymbol{C}_r \Delta(\boldsymbol{\varepsilon}_{\text{mech}} - \boldsymbol{\varepsilon}) - \sigma_{\text{res}}(t), \ \forall\ T \geq T_g(\varrho) \\ \boldsymbol{C}_g \Delta(\boldsymbol{\varepsilon}_{\text{mech}} - \boldsymbol{\varepsilon}), \ \forall\ T < T_g(\varrho) \end{cases} \tag{7}$$

Finally, the evolving locked-in residual stress, based on the loading history, is calculated as

$$\boldsymbol{\sigma}_{\text{res}}(t + \Delta t) = \begin{cases} 0, \ \forall\ T \geq T_g(\varrho) \\ \boldsymbol{\sigma}_{\text{res}}(t) + (\boldsymbol{C}_g - \boldsymbol{C}_r)\Delta(\boldsymbol{\varepsilon}_{\text{mech}} - \boldsymbol{\varepsilon}), \ \forall\ T < T_g(\varrho) \end{cases} \tag{8}$$

The state variable, denoted as $\boldsymbol{\sigma}_{\text{res}}$, is calculated based on the loading conditions and the evolution of cure-state variables. In the rubbery and viscous states, the material is considered to be relaxed, and as a result, $\boldsymbol{\sigma}_{\text{res}}$ is set to 0. However, in the glassy state, an internal stress builds up gradually. This accumulated stress is eventually released at the boundaries once the curing process is complete, causing plastic deformations. The residual state remaining within the part is denoted by $(\boldsymbol{\sigma}_{\text{res}}, \boldsymbol{\varepsilon}_{\text{res}})$ and is initialized for the consecutive structural numerical analyses. Note that residual state redistribution is not addressed, as it is relevant when machining processes occur after manufacturing.

2.2. Phase Field Model

The PF model is developed from a thermodynamic framework in which cracks propagate when the fracture toughness exceeds the critical material toughness [41,42]. A diffuse region of finite width characterizing the discrete crack surface is implemented using a variable, ϕ, where ϕ = [0,1] ranges from zero to one, representing the damaged and undamaged states, respectively [43,44]. A detailed PF approximation of smeared crack topology is provided in Appendix B. The composite lamina, Ω, with fibers oriented at an angle, θ, includes a sharp crack, Γ, with a residual state $(\boldsymbol{\sigma}_{\text{res}}, \boldsymbol{\varepsilon}_{\text{res}})$, as illustrated in Figure 1.

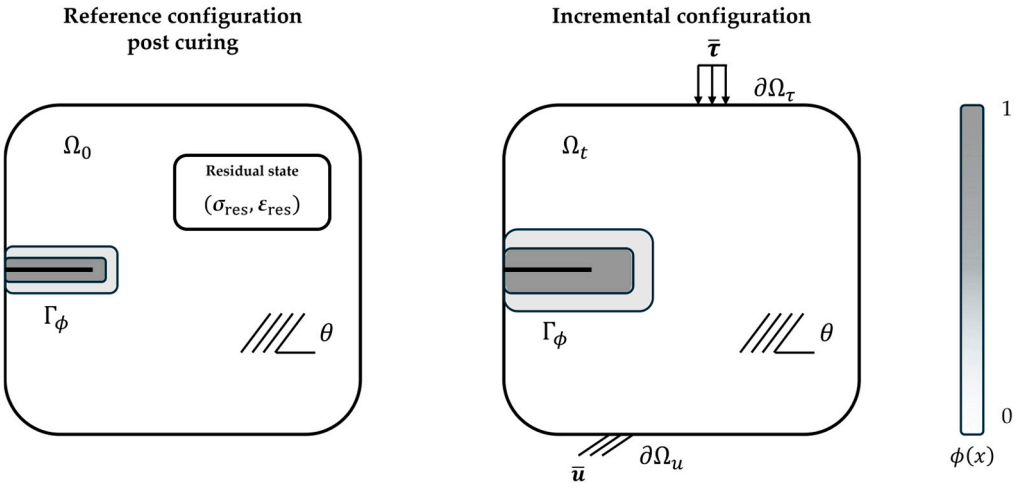

Figure 1. Residually stressed composite lamina, Ω, at reference and incremental configuration.

The lamina, Ω, is associated with boundary conditions represented by $\partial\Omega_u$ and $\partial\Omega_\tau$, and $\partial\Omega_u \bigcup \partial\Omega_\tau = \partial\Omega, \partial\Omega_u \bigcap \partial\Omega_\tau = \{\}$. The regularized crack functional is given by

$$\begin{gathered} \Gamma_\phi = \int_\Omega \gamma(\phi, \nabla\phi; \boldsymbol{A}) d\Omega \\ \gamma(\phi, \nabla\phi; \boldsymbol{A}) = \frac{1}{c_0}\left(\frac{1}{l_\phi}\omega(\phi) + l_\phi \boldsymbol{A} : \nabla\phi \otimes \nabla\phi\right) \end{gathered} \tag{9}$$

where $\gamma(\phi, \nabla\phi; \boldsymbol{A})$ signifies the energy density of the crack surface per unit volume, l_ϕ denotes the regularization length scale, and $\omega(\phi)$ refers to the geometric function. The constant c_0 is defined as $c_0 = 4\int_0^1 \sqrt{\omega(\phi)}d\phi$. The generic form of $\omega(\phi)$ is taken as $\zeta\phi + (1-\zeta)\phi^2 \; \forall \; \phi \in [0,1]$. $\boldsymbol{A}$ is the second-order structural tensor that accounts for the anisotropy, defined as $\boldsymbol{A} = \boldsymbol{I} + \varsigma\boldsymbol{M}$, where ς is the anisotropic constant that penalizes damage normal to the unit normal vector, $\boldsymbol{M}$, which depends on the critical fracture toughness in both strong and weak directions. The material direction is denoted by $\boldsymbol{m} = [\cos\theta, \sin\theta, 0\,]^T$, and $\boldsymbol{M} = \boldsymbol{m} \otimes \boldsymbol{m}$. The surface fracture energy is given by

$$W_\phi = \int_\Gamma G_c dA \; = \int_\Omega G_c \gamma(\phi, \nabla\phi; \boldsymbol{A}) d\Omega \tag{10}$$

Based on the variational framework [68], the regularized total energy functional is defined as the combination of the elastic potential energy, the fracture energy associated with the crack surface, and the work influenced by external loads, as given by

$$W = \int_\Omega g(\phi)\psi d\Omega + \int_\Omega G_c \gamma(\phi, \nabla\phi; \boldsymbol{A}) d\Omega - \int_\Omega \boldsymbol{b}\cdot\boldsymbol{u} d\Omega - \int_{\partial\Omega} \overline{\boldsymbol{\tau}}\cdot\boldsymbol{u} d\mathrm{A} \tag{11}$$

where ψ represent the Helmholtz free energy function, and $\boldsymbol{b}$ and $\overline{\boldsymbol{\tau}}$ represent the body force and surface traction, respectively. The degradation function, $g(\phi)$, is designed to account for material degradation due to cracks and must meet the following conditions:

$$g(0) = 1, g(1) = 0, g'(\phi) < 0 \text{ and } g'(1) = 0 \tag{12}$$

The choice of $g(\phi)$ and $\omega(\phi)$ has led to the adoption of various PF models for composites in recent years [69,70]. The three most popular degradation functions, namely, the Ambrosio–Tortorelli functions (AT1 and AT2) and the Phase Field Cohesive Zone (PF-CZ) functions, along with their respective characteristics, are presented in Table 1. In the AT2 model, while damage boundedness is inherently guaranteed, it does not include an elastic domain, leading to immediate damage regardless of the load magnitude, which is unrealistic. In contrast, the AT1 and PF-CZ models overcome this limitation by introducing an elastic domain with a defined damage threshold, as specified by

$$\begin{cases} \gamma_{th} = \frac{3G_c}{16 l_\phi} \text{ (for AT1 model)} \\ \gamma_{th} = \frac{{f_t}^2}{2E'} \text{(for PF-CZ model)} \end{cases} \tag{13}$$

Table 1. Different geometric and degradation functions, along with their associated properties.

Characteristics	Ambrosio–Tortorelli Type 1 (AT1)	Ambrosio–Tortorelli Type 2 (AT1)	Phase Field Cohesive Zone (PF-CZ) [1]
Damage type	brittle	brittle	brittle-cohesive
Damage profile	$\left(1 - \frac{\lvert x\rvert}{2l_\phi}\right)^2$	$e^{\left(-\frac{\lvert x\rvert}{l_\phi}\right)}$	$1 - \sin\left(1 - \frac{\lvert x\rvert}{l_\phi}\right)$
Damage bandwidth	$4l_\phi$	∞	πl_ϕ
$\omega(\phi)$	ϕ	ϕ^2	$2\phi - \phi^2$
$g(\phi)$	$(1-\phi)^2$	$(1-\phi)^2$	$\frac{(1-\phi)^p}{(1-\phi)^p + Q(\phi)}$
c_0	2.67	2	π

[1] For the PF-CZ model, $Q(\phi) = \left(1 + z_1\phi + z_2 z_3 \phi^2\right)$ and $z_1 = \frac{4}{\pi l_\phi}.E'{G_c}'/{f_t}^2$. The values of p, z_2, and z_3 vary depending on the specific traction-separation law [69]. Here, $E', {G_c}'$, and f_t represent the modulus, critical fracture toughness, and material tensile strength in the weak direction of the homogeneous meso-scale lamina, respectively.

In this study, the AT1 degradation type regularization is employed to define a finite width for the diffuse interlaminar and intralaminar cracks, given the inherently brittle nature of UD thermoset composites. With the cure-induced residual state, represented by $(\boldsymbol{\sigma}_{\text{res}},\ \boldsymbol{\varepsilon}_{\text{res}})$, the elastic residual strain, $\boldsymbol{\varepsilon}_{\text{res}}$, is known in advance and is incorporated into the

strain determination as an offset, expressed as: $\boldsymbol{\varepsilon}^* = \boldsymbol{\varepsilon}_{\text{mech}} + \boldsymbol{\varepsilon}_{\text{res}}$. The effective Helmholtz free energy, ψ, is defined as follows:

$$\begin{gathered}\psi = \tfrac{1}{2}\boldsymbol{\varepsilon}^* : \boldsymbol{C} : \boldsymbol{\varepsilon}^* = \tfrac{1}{2}\, o_1 tr^2(\boldsymbol{\varepsilon}^*) + \, o_2 tr\left(\boldsymbol{\varepsilon}^{*2}\right) \\ + o_3 tr(\boldsymbol{\varepsilon}^*) tr(\boldsymbol{\varepsilon}^* \boldsymbol{M}) + 2(o_4 - o_2) tr\left(\boldsymbol{\varepsilon}^{*2}\boldsymbol{M}\right) + \tfrac{1}{2} o_5 tr^2(\boldsymbol{\varepsilon}^* \boldsymbol{M})\end{gathered} \tag{14}$$

where $o_{i=1,2,\ldots 5}$ are constants dependent on the mechanical properties of the UD composite lamina [71]. The parameters are dependent on the modulus, $\boldsymbol{C}$, which in turn is related to the mechanical properties. This dependency is briefly explained in Appendix C. Note that when $o_2 = o_4$ and $o_3 = o_5 = 0$, the condition reverts back to the case of isotropy, which is ideal for modeling the interface with homogeneous isotropic resin. The volumetric–deviatoric split corresponding to the isotropic part is used for modeling mixed-mode fracture [72,73]. The decomposition of the isotropic component of the effective Helmholtz free energy is given as

$$\psi^{+}_{\text{iso}} = \frac{K}{2} < tr(\boldsymbol{\varepsilon}^*) >^2_{+} + \mu_T(\boldsymbol{\varepsilon}^*_D : \boldsymbol{\varepsilon}^*_D); \quad \psi^{-}_{\text{iso}} = \frac{K}{2} < tr(\boldsymbol{\varepsilon}^*) >^2_{-} \tag{15}$$

where K is the bulk modulus given by $K = o_1 + (2/3)o_2$, and $\boldsymbol{\varepsilon}^*_D = \boldsymbol{\varepsilon}^* - (1/3)tr(\boldsymbol{\varepsilon}^*)$ represents the deviatoric component of the effective strain in the system. The Macaulay bracket is defined as $< d >_{\pm} = (d \pm |d|)/2$. The decomposition of the of the anisotropic part is given by

$$\begin{gathered}\psi^{\pm}_{\text{aniso}} = o_3 < tr(\boldsymbol{\varepsilon}^*) >_{\pm} < tr(\boldsymbol{\varepsilon}^* \boldsymbol{M}) >_{\pm} + 2(o_4 - o_2) < tr\left(\boldsymbol{\varepsilon}^{*2}\boldsymbol{M}\right) >_{\pm} \\ + \tfrac{1}{2} o_5 < tr(\boldsymbol{\varepsilon}^* \boldsymbol{M}) >^2_{\pm}\end{gathered} \tag{16}$$

As ϕ evolves, elastic energy is degraded according to $g(\phi)$, and, consequently, the stress state is expressed as

$$\boldsymbol{\sigma} = g(\phi)(\boldsymbol{\sigma}_{\text{res}} + \boldsymbol{C} : \, \boldsymbol{\varepsilon}_{\text{mech}}) \tag{17}$$

The initial residual stress state is assumed to remain unchanged after the demolding step in the cure analysis. However, as cracks propagate, the stress state changes due to the degradation of the total stress, which also affects the residual stresses. The variation of the system's regularized total energy functional, W, with respect to displacement, u, and damage, ϕ, produces the core equations of the PF model:

$$\begin{cases} \nabla \boldsymbol{\sigma} + \boldsymbol{b} = 0 \text{ in } \Omega \\ g'(\phi) H + \left(\frac{1}{c_0} \left(\frac{\omega(\phi)}{l_\phi} - 2 l_\phi \nabla \phi \cdot (\boldsymbol{A} \cdot \nabla \phi) \right) \right) \geq 0, \; \dot{\phi} \; \geq 0 \text{ in } \Omega \\ \boldsymbol{\sigma} . \, \boldsymbol{n_v} = \overline{\boldsymbol{\tau}} \text{ in } \partial\Omega_\tau \\ \nabla \phi \, . \; \boldsymbol{n_v} = 0 \text{ in } \partial\Omega_u \end{cases} \tag{18}$$

where $\boldsymbol{n_v}$ represents the unit normal vector. The damage driving force, $\mathcal{H}$, is defined as follows:

$$\mathcal{H} = \frac{\psi^{+}_{\text{aniso}} \sqrt{\varsigma + 1}}{G^f_c} + \frac{\psi^{+}_{m_I}}{G^{m_I}_c} + \frac{\psi^{+}_{m_{II}}}{G^{m_{II}}_c} \tag{19}$$

where G^f_c corresponds to the fracture toughness associated with fiber failure, while $G^{m_I}_c$ and $G^{m_{II}}_c$ represent the critical toughness due to mode I and mode II crack propagation, respectively. Figure 2 illustrates the various types of failures that can occur in composite structures when subjected to loads. This definition of $\mathcal{H}$ facilitates precise modeling of composite failures under different modes [49]. It is important to note that damage is an irreversible process; thus, the PF evolution law in Equation (18) must satisfy the condition

$\dot{\phi} \geq 0$. To ensure this, the definition of the history variable, $\mathcal{H}$, must comply with the Karush–Kuhn–Tucker conditions, which are given by

$$\begin{gathered} \psi_i^+ - \mathcal{H} \leq 0,\ \dot{\mathcal{H}} \geq 0,\ \mathcal{H}_i(\psi_i^+ - \mathcal{H}_i) = 0 \quad \text{with } i = f, m_I,\ m_{II} \\ \mathcal{H}_i = \max_{t\epsilon[0,t_{\text{tot}}]} \psi_i^+ \end{gathered} \tag{20}$$

where t and t_{tot} represent the current time and total time, respectively. $\mathcal{H}_{m_I}$ and $\mathcal{H}_{m_{II}}$ are the driving forces for mode I and mode II crack propagation, respectively. This criterion establishes the propagation conditions for inter- and intralaminar cracks within the composite material. A mode I-dominated mixed-mode propagation occurs when $\mathcal{H}_{m_I} > \mathcal{H}_{m_{II}}$, while the opposite is true for mode II-dominated propagation.

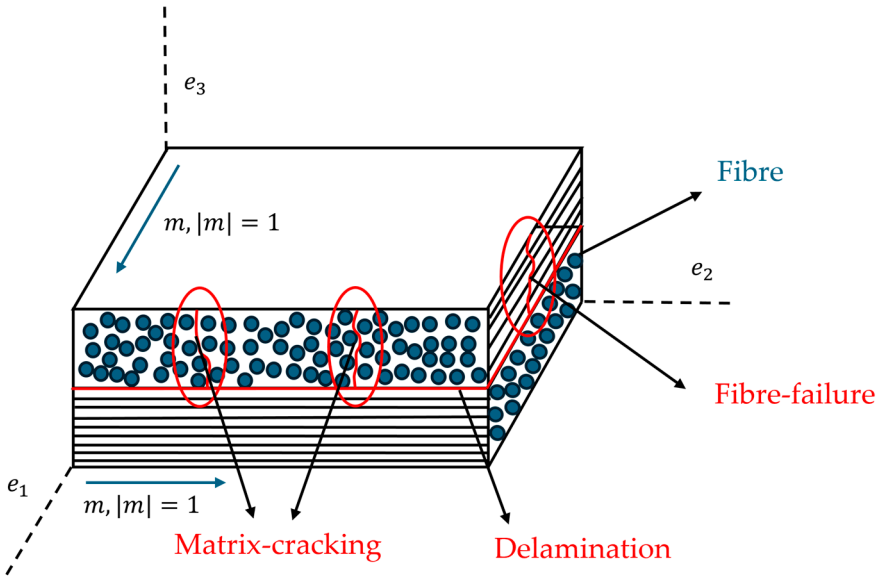

Figure 2. Schematic overview of a laminate, highlighting the different failures.

Remark 1. *Significance of the anisotropic constant, ς, and the length scale, l_ϕ, in UD composites.*

Considering a failure crack that propagates at an angle, χ, with respect to the global system, the gradient of the crack in the normal direction is expressed as follows: $\nabla^T\phi = ||\nabla\phi||^2[-sin\chi, cos\chi, 0\,]$. With the definition of the structural tensor, $\boldsymbol{A}$, the anisotropic part of the surface energy density is given by

$$\begin{gathered} \nabla\phi{\cdot}\boldsymbol{A}{\cdot}\nabla\phi = ||\nabla\phi||^2\boldsymbol{A}(\chi) \\ \text{where, } \boldsymbol{A}(\chi) = \left(1 + \tfrac{\varsigma}{2}\right) - \tfrac{\varsigma}{2}cos(2(\chi - \theta)) \end{gathered} \tag{21}$$

It is important to note that when χ aligns with θ, $\boldsymbol{A}(\chi)$ equals 1; otherwise, $\boldsymbol{A}(\chi) > 1$, $\forall\ \varsigma > 0$. By defining the anisotropic fracture energy as $G_c(\chi) = G_c\sqrt{\boldsymbol{A}(\chi)}$ and length scale as $l_\phi(\chi) = l_\phi\sqrt{\boldsymbol{A}(\chi)}$, the crack surface fracture energy, referring to Equation (10), can be rewritten as follows:

$$W_\phi = \int_\Omega \frac{G_c(\chi)}{c_0}\left(\frac{1}{l_\phi(\chi)}\omega(\phi) + l_\phi(\chi)||\nabla\phi||^2\right) d\Omega \tag{22}$$

With this formulation, the influence of the parameter ς and the fiber direction θ is further investigated. From the literature, the value of ς should satisfy $\left(G_c^f / G_c^{m_I/m_{II}}\right)^2 - 1$. Unfortunately, the difference in fracture toughness between the matrix and fibers for the case of UD composites is quite large, resulting in an unreasonably high value for ς. This, in turn, leads to numerical stability issues and/or diffusive failure when the crack is

perpendicular to the fiber direction. Therefore, the parameter ς = {0–50} was chosen for a trial-and-error approach to calibration. We considered the experimental case of a Single Edge Notched lamina with dimensions 1 mm × 2 mm, featuring fibers oriented at different angles (30°, 45°, and 60°), as shown in study [74]. The material under investigation is Hexcel's HTA/6376 epoxy. The bottom of the lamina was fixed, while a displacement load was applied to the top. Testing was conducted using a Zwick/Roell 100 kN universal testing machine, with the load applied at a rate of 0.1 mm/s. High-speed camera equipment was employed to capture images of the resulting failures. The material properties utilized in the analysis were as follows: longitudinal modulus E_X = 114,880 MPa, transverse modulus E_Y = 11,700 MPa, shear modulus G_{XY} = 9660 MPa, Poisson's ratio μ_{XY} = 0.21, fiber failure toughness G_c^f = 106.30 N/mm, critical fracture toughness in mode I $G_c^{m_I}$ = 0.28 N/mm and critical fracture toughness in mode II $G_c^{m_{II}}$ = 0.79 N/mm. An internal length scale of l_ϕ = 0.02 mm was taken with element size set to $l_\phi/5$. It was observed that as ς increased, the minimum fracture energy occurred along the fiber direction, which facilitated crack propagation in that direction. This behavior aligns with experimental findings and is depicted in Figure 3A–C. However, it is crucial to ensure that the value of ς remains sufficiently small to achieve a well-defined smeared crack pattern. Therefore, for the subsequent numerical analyses involving UD composite laminates, ς was assumed to be 50, although it should be calibrated for different composite materials. Furthermore, the influence of increasing ς on peak loads and failure displacement can be observed in Figure 3D. Furthermore, for a fixed value of ς = 50, the influence of the internal length scale, l_ϕ, was investigated. According to the literature, l_ϕ is a material-dependent parameter that also depends on the geometric and degradation functions implemented within the PF model. In this study, the AT1 model was adopted and l_ϕ was estimated as in [46]:

$$l_\phi = \frac{3E'G_c{}'}{8f_t{}^2} \tag{23}$$

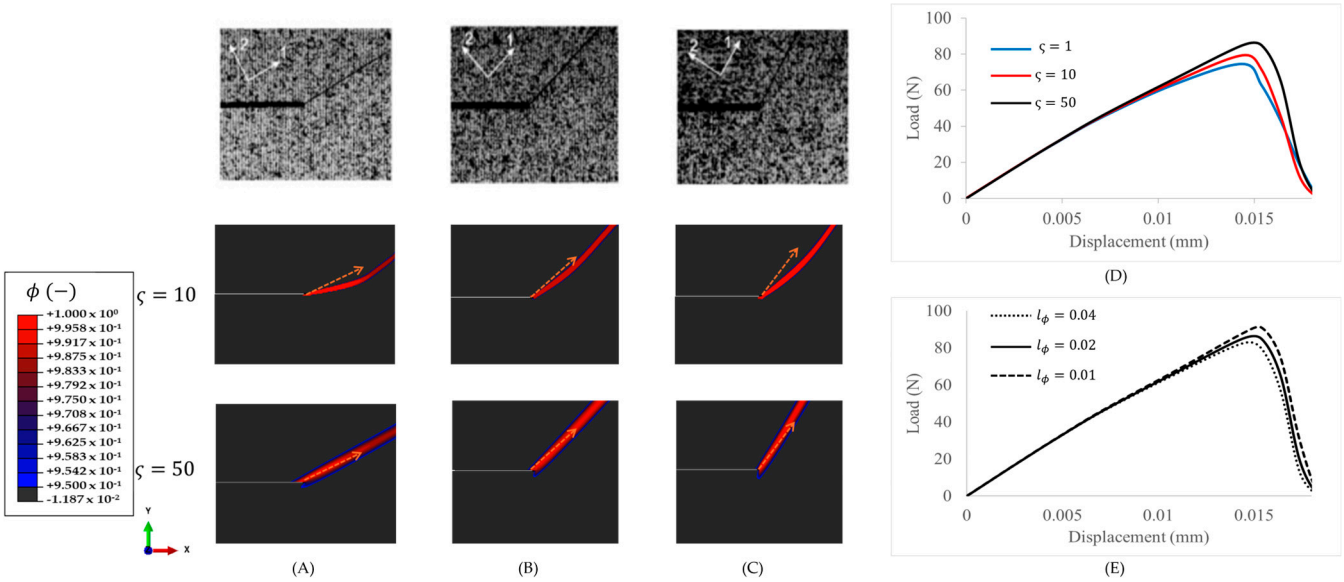

Figure 3. Effect of anisotropic parameter, ς, on the crack pattern for different fiber orientations represented experimentally in 1-direction and numerically by orange arrows relative to the X-axis: (**A**) at 30°, (**B**) at 45°, and (**C**) at 60° (with a deformation scaling factor of 1.0). Additionally, (**D**) presents the comparison of load-displacement plot for 45° case. All computations were conducted with a length scale of l_ϕ = 0.02 mm. (**E**) illustrates the influence of the length scale l_ϕ with a fixed value of ς = 50 for 45° case. Experimental results from [74] were reproduced with permission from Elsevier.

The f_t is unknown from experiments and was assumed to range between 150 and 350 MPa, within which l_ϕ = {0.01–0.04} was explored. The numerical predictions were observed to be stable, with only a slight influence of l_ϕ on the mechanical response, as shown in Figure 3E.

2.3. Numerical Implementation

In this section, we present the implementation of the coupled computational framework proposed in this study. The numerical analysis using the CHILE model includes FE calculations carried out with ABAQUS/Standard, along with a User Material subroutine (UMAT). This model enables superposition between cure-state variables and loading conditions, as explained in Section 2.1. Following the completion of the curing step, the demolding process is introduced to capture the residual state of the part after manufacturing. After demolding, the structural numerical model incorporating the PF model with cure-induced residual stress is implemented using different UMAT. In this context, the concept of heat transfer analogy [75,76] is implemented within the UMAT associated with the PF model. The analogy is as follows: for a body with thermal conductivity $\boldsymbol{\lambda}$, and in the presence of a heat source r, the steady-state evolution of the temperature field T is governed by the balance law:

$$\boldsymbol{\lambda} \cdot \nabla^2 T = -r \tag{24}$$

By rearranging the PF evolution law (refer to Equation (18)) and treating damage as analogous to temperature, the equation can be expressed as follows:

$$\boldsymbol{A} \cdot \nabla^2 \phi = -r = \frac{g'(\phi)\mathcal{H}}{l_\phi} + \frac{\phi}{{l_\phi}^2} \text{ in } \Omega \tag{25}$$

The heat flux and its rate are defined within the HETVAL subroutine for computing the Jacobian matrix. The primary motivation for employing the heat-transfer analogy was its ability to seamlessly integrate the residual cure stress field alongside the initial cracks, defined with nodal temperature, i.e., $\phi > 0.97$. The CHILE model, which includes initial cracks, does not effectively constrain the cure boundary conditions. In contrast, introducing an initial crack solely within the PF model results in a loss of information regarding the localized cure-induced residual stress state. Additionally, the effects of stochastic voids can be incorporated within the coupled framework using this heat transfer analogy.

The global system equations outlined in the PF model (refer to Section 2.2) can be solved using either a monolithic or staggered scheme. In the staggered scheme, as opposed to the monolithic approach, the PF and the displacement sub-equations in Equation (18) are separated by keeping the history variable fixed during the solution of the displacement problem. Although the monolithic solution is stable, it often suffers from poor convergence. In contrast, the staggered scheme is more robust but requires small increments to maintain the numerical stability of the FE solution. The latter is preferred for PF numerical analysis, especially when stochastic voids are included within the coupled framework. For post-processing the PF numerical results, particularly the nodal temperature to compute failure probability, the tools in study [77] were utilized.

3. Results and Discussion

In this section, we first benchmark the numerical computational models against experimental data. We then implement the proposed coupled CHILE-PF computational framework on an example of L-shaped parts. The thicknesses selected for the numerical analyses of UD laminates in this study range from 2 mm to 20 mm, encompassing typical fuselage and wing-skin-associated features. The material under consideration was the AS4/8552 UD carbon/epoxy prepreg [78]. Each ply in the stacking configuration had a thickness of 0.183 mm. Additionally, interfaces, denoted by "//", were assumed to have a finite thickness of 0.02 mm between dissimilar plies.

The numerical analyses for the following examples were conducted at the meso-scale, assuming that the fiber–resin matrix corresponding to each ply was homogeneous. In the initial cure analysis associated with the CHILE model, several assumptions were taken into account. The diffusion cure kinetics model [13,79] was utilized to update the cure-state variables. It was assumed that the temperature was evenly distributed across the entire part. Furthermore, it was assumed that the thermo-chemo-mechanical properties remained constant across different cure states and that there was sufficient stress buildup within the viscous state during polymerization. The CTE and CCS were considered independent of the degree of cure due to their minimal variations. This is because thermal expansion is primarily driven by temperature changes rather than small variations in the cure, and most chemical shrinkage occurs during the early stages before gelation.

Secondly, from the perspective of structural PF numerical analysis, the examples involve displacement-loading conditions. With the inclusion of interfaces between dissimilar plies, an additional PF variable corresponding to the interface was considered to model interlaminar delamination. The critical fracture toughness attributed to the fibers was G_c^f = 71.90 N/mm, while the critical fracture toughness for the matrix in the normal and shear directions were $G_c^{m_I}$ = 0.305 N/mm and $G_c^{m_{II}}$ = 2.77 N/mm, respectively. The anisotropic parameter ς was taken as 50. A length scale parameter, l_ϕ = 0.1, was assumed for both inter- and intralaminar failures. It was assumed that the homogeneous isotropic interface modelled with the initial crack was weak, with a fracture toughness of (1/50)th of the $G_c^{m_I}$ and $G_c^{m_{II}}$ compared to that of the surrounding bulk UD lamina. This occurs because the matrix-rich region has lower resistance to failure, causing microcracks to form and propagate along the interfaces, which leads to a reduction in the load-carrying capacity. Given the significant differences in fracture toughness between the plies and interfaces, a bottleneck issue arises. This issue is addressed by replacing the abrupt transition with a continuous and smooth function that defines such drastic changes [50]. It is crucial to emphasize that when applying the first gradient of damage in the PF approach for regularization, a minimum FE mesh size is necessary to accurately capture the topology of the regularized crack surface (refer to Appendix B). Therefore, a characteristic element size of $l_\phi/4$ was assumed for the FE discretization along the predicted failure propagation paths [80]. The numerical analysis, which included both a cure and a structural analysis, was performed using ABAQUS/CAE (Version 2023), integrated with two FORTRAN UMATs that ran consecutively. The coupled computational numerical runs utilized six CPU cores per job and were executed on the in-house supercomputer, Lucia.

3.1. Benchmark for CHILE Numerical Model

The experimental analysis involved a Z-shaped part fabricated using the hand-layup method with the configuration [45°//−45°//0°//90°] s. The part was cured in an autoclave under a temperature cycle that began with a heating ramp of 1.50 °C per minute, gradually increasing the temperature from room temperature to 180 °C. Upon reaching 180 °C, the component was held at this temperature for 120 min. After the dwell period, the part was cooled back to room temperature at the same rate of 1.50 °C per minute. Throughout the entire curing cycle, a constant pressure of 7 bars was applied. The specimen was manufactured using an invar mold. After demolding, the spring-in angles were measured using point cloud data collected with a Nikon MMDx100 laser scanner (Nikon Metrology Europe S.A., Leuven, Belgium). The FE model, illustrated in Figure 4, considers the pressure and temperature cure cycles applied to the free surface of the Z-shaped part. The 3D geometrical model was created by extruding and meshing the defined shell geometry in the thickness direction. Prior to extrusion, the materials, thicknesses, and orientations of the plies were defined. Draping modeling was performed using a Simulayt Composite Modeller within ABAQUS. The Z-shaped part in the 3D model was discretized into 17,784 hexahedral C3D8 elements, each defined with a linear geometric order and assigned specific local orientations to accurately represent the composite layup. The mold,

designed as a rigid body, was constructed using 2296 quadrilateral R3D4 elements, also characterized by a linear geometric order.

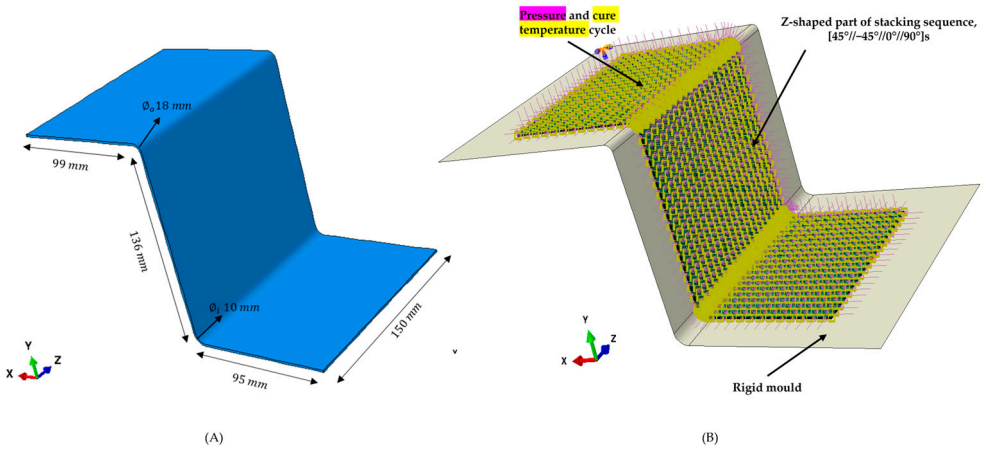

Figure 4. (**A**) Geometry and (**B**) FE model with associated boundary conditions for the curing analysis of the Z-shaped part.

The purpose of the imposed boundary condition, as shown in Figure 4 of the numerical model, was to closely replicate the experimental conditions, where pressure holds the part against the mold, preventing the curved section from closing freely. Finally, during the demolding step, the pressure and contact conditions with the mold were removed to predict distortions. Additionally, specific constraints were applied to three corners of the specimen during the demolding step to prevent rigid body movements. The mechanical and thermo-chemical properties of the UD AS4/8552 and the 8552 resin, related to the bulk plies and interfaces, respectively, are detailed in Tables 2 and 3.

Table 2. Properties of UD prepreg AS4/8552 at various states [78,81,82].

Properties	Uni-Directional Plies	
	Rubbery	**Glassy**
Longitudinal modulus, E_X (MPa)	137,665.50	137,770.70
Transitional slope for E_X (MPa/°C)		3.43
Transversal modulus, E_Y (MPa)	165	7070.70
Transitional slope for E_Y (MPa/°C)		13.51
Transversal modulus, E_Z (MPa)	165	7070.70
Transitional slope for E_Z (MPa/°C)		13.51
In-plane shear modulus, G_{XY} (MPa)	44.30	3404.40
Transitional slope for G_{XY} (MPa/°C)		12.50
Out-of-plane shear modulus, G_{XZ} (MPa)	44.30	3404.40
Transitional slope for G_{XZ} (MPa/°C)		12.50
Out-of-plane shear modulus, G_{YX} (MPa)	41.60	2594.10
Transitional slope for G_{YX} (MPa/°C)		5.77
In-plane Poisson's ratio, μ_{ZY} (-)	4.00×10^{-4}	1.89×10^{-2}
Out-of-plane Poisson's ratio, μ_{XY} (-)	4.00×10^{-4}	1.89×10^{-2}
Out-of-plane Poisson's ratio, μ_{ZY} (-)	0.98	0.45
CTE in longitudinal direction, α_X (1/°C)	-8.78×10^{-7}	-7.98×10^{-8}
CTE in transverse direction, α_Z (1/°C)	4.06×10^{-5}	3.05×10^{-5}
CTE in through thickness direction, α_Y (1/°C)	4.06×10^{-5}	3.05×10^{-5}
CCS in longitudinal direction, β_X (-)	1.07×10^{-4}	6.97×10^{-3}
CCS in transverse direction, β_Z (-)	-1.82×10^{-2}	-1.80×10^{-2}
CCS in through thickness direction, β_Y (-)	-1.82×10^{-2}	-1.80×10^{-2}

Table 3. Properties of homogeneous resin 8552 at various states [78].

Properties	Uni-Directional Plies	
	Rubbery	**Glassy**
Modulus, E (MPa)	40.30	2328.87
Transitional slope for E (MPa/°C)		8.07
Shear modulus, G (MPa)	13.44	868.30
Transitional slope for G (MPa/°C)		3.95
Poisson's ratio, μ (-)	4.90×10^{-1}	3.70×10^{-1}
CTE in longitudinal direction, α (1/°C)	1.50×10^{-4}	4.89×10^{-5}
CCS in through thickness direction, β (−)	8.30×10^{-1}	7.60×10^{-1}

The cure-induced residual stress fields upon demolding, as determined by the CHILE numerical model, are crucial because this state of stress persists after manufacturing and can potentially affect the final strength of the component. The cure kinetics model [79] describes the evolution of cure state variables, which, in turn, informs the development of properties during the curing process at various states. More details on the parameters of the cure kinetics model and their impact on stress buildup can be found in our previous work [83,84]. As the vitrification process begins, the substantial enhancement of mechanical properties becomes coupled with volumetric free strains, leading to the formation of tensile residual stresses within the flanges and web. Figure 5 illustrates the residual stresses in the global X, Y, and Z directions upon demolding. When the boundary conditions are removed during the demolding step, most of the induced residual stress is released, resulting in distortions manifested as spring-in angles A_1 and A_2. It is important to note that there is a significant magnitude of tensile residual stresses at the corners, particularly along the global Y-axis, reaching up to 32 MPa. Moreover, the induced residual stresses are unevenly distributed throughout the thickness of the part. This influence should not be overlooked in the subsequent structural analysis within the virtual manufacturing framework.

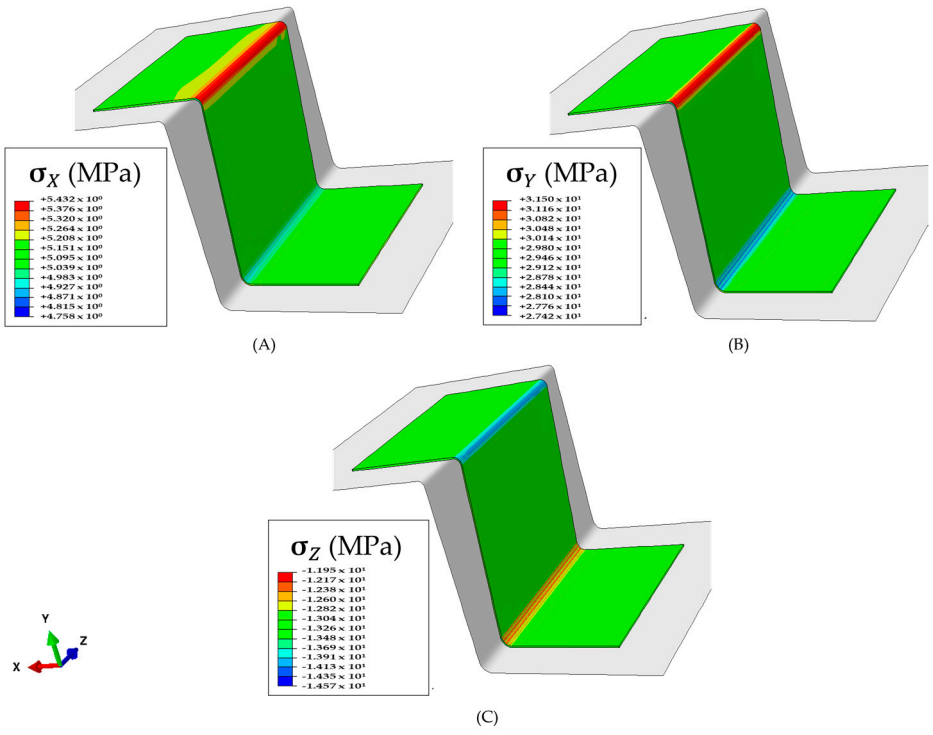

Figure 5. Residual stress upon the demolding step occurs in the primary global directions: (**A**) X direction, (**B**) Y direction, and (**C**) Z direction (with a deformation scaling factor of 1.0).

Validation of the CHILE model was achieved by comparing the spring-in angles resulting from process-induced distortions. It was observed that these experimental measurements were associated with a standard deviation of 0.2. Figure 6 shows the comparison of the average values of spring-in angles A_1 and A_2 after the demolding step. The numerical analysis predicted a relative error of 19.75% and 17.27% for angles A_1 and A_2, respectively. The total CPU time required for the analysis was approximately 0.61 h. Given the closer correlation with the measurements from the laser scans, the model is further implemented to the case study of L-shaped specimens in Section 3.3, which feature localized regions with a comparable type of curvature.

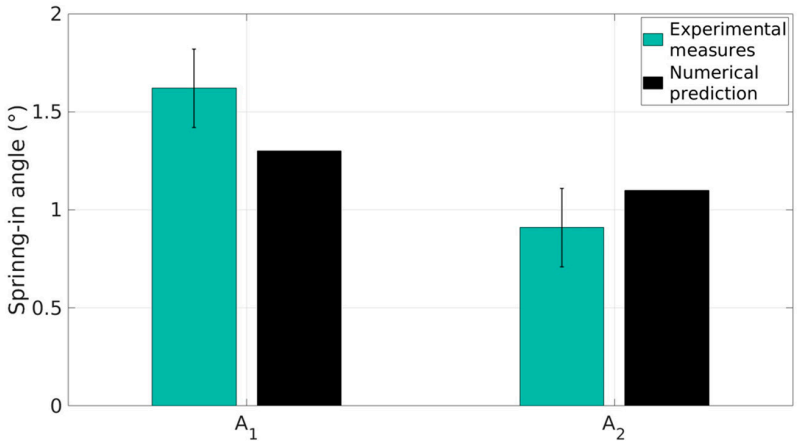

Figure 6. Comparison of spring-in measurements between experimental laser scans and CHILE numerical post-processing.

3.2. Benchmark for PF Numerical Model

Just as we validated the CHILE model, we also validated the PF model for simulating failure in pure mode I and mode II cases. This behavior in mode I and mode II was represented using Double Cantilever Beam (DCB) and End-Notch Flexure (ENF) tests, respectively. The DCB and ENF tests were conducted according to ASTM D5528 and D7905/7905M standards [85,86], respectively. A 50 kN load cell was employed, with a loading rate of 1 mm/min. Specimens with nominal pre-crack lengths of 35 mm and 32 mm across the width were used for DCB and ENF tests, respectively. More details on the experiments can be found in the literature [87,88]. The experimental analysis consisted of laminates made exclusively of 0° plies. In this pure UD configuration, the residual stress field resulting from manufacturing was found to have an insignificant influence and was therefore excluded from the subsequent PF numerical analysis. This was due to the lack of mismatch in the CTEs and CCSs between adjacent laminas. The effective properties were calculated after the cooling stage of manufacturing, with cooling rates as shown in Tables 2 and 3.

Firstly, for the case of mode I failure, a conventional DCB benchmark specimen with reinforcement plates bonded to each arm was used for analysis. The specimen labeled $[0°_{16}]$ measured 175 mm in length and 3 mm in thickness. The reinforcements, each labeled $[0°_8]$, measured 120 mm in length and 1.47 mm in thickness, and were positioned on either side of the arm to induce curvature in the delamination front during propagation. Figure 7A illustrates the specimen's configuration and the corresponding boundary conditions. In the FE model, the part was represented by 266,080 hexahedral C3D8T elements with linear geometric order. The final position of the delamination front after a prescribed displacement of 15 mm is shown in Figure 7B. The peak load occurred during the elastic opening of the specimen's arms, just prior to crack propagation (around 3 mm), reaching approximately 180.84 N, as noted in the experiments. In contrast, further interlaminar crack propagation caused the load to decrease with displacement until the delamination reached the reinforced section, where the load began to increase, reaching 168.85 N due to

the stiffness provided by the reinforcements. The PF numerical analysis predicted an initial peak load of 180.37 N and a subsequent peak load of 157.04 N, with errors of 0.26% and 6.99%, respectively. Furthermore, the PF numerical model replicated the loading–unloading boundary condition at every 1 mm of accumulated displacement opening, showing a strong correlation with the delamination fronts, as shown in Figure 8.

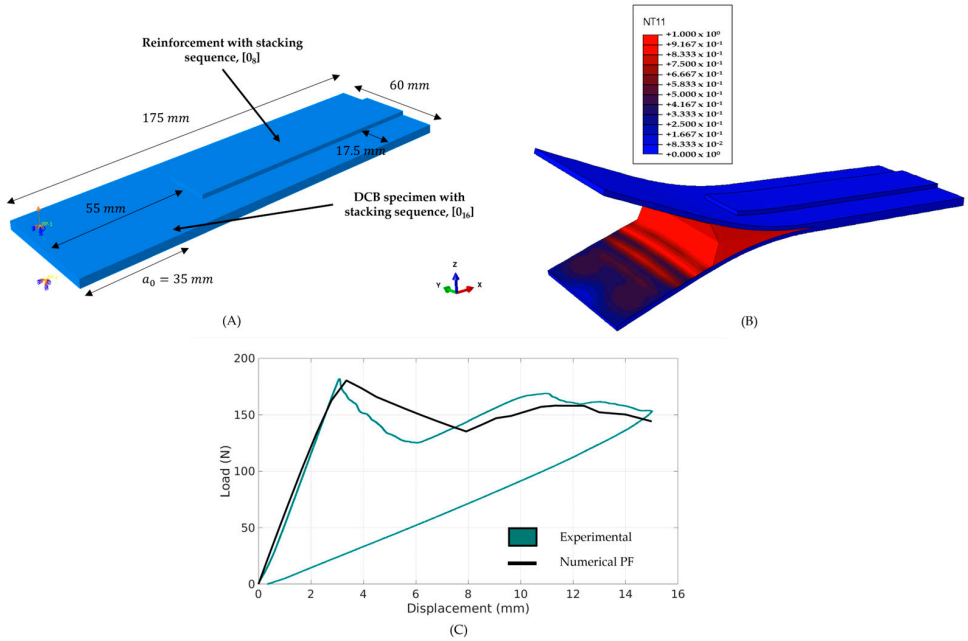

Figure 7. (**A**) Geometry and boundary conditions for the Mode I test, (**B**) evolution of damage along the interface with a scaling factor of 5.0, and (**C**) comparison of the load-displacement plot between experimental data [87] and the PF numerical model.

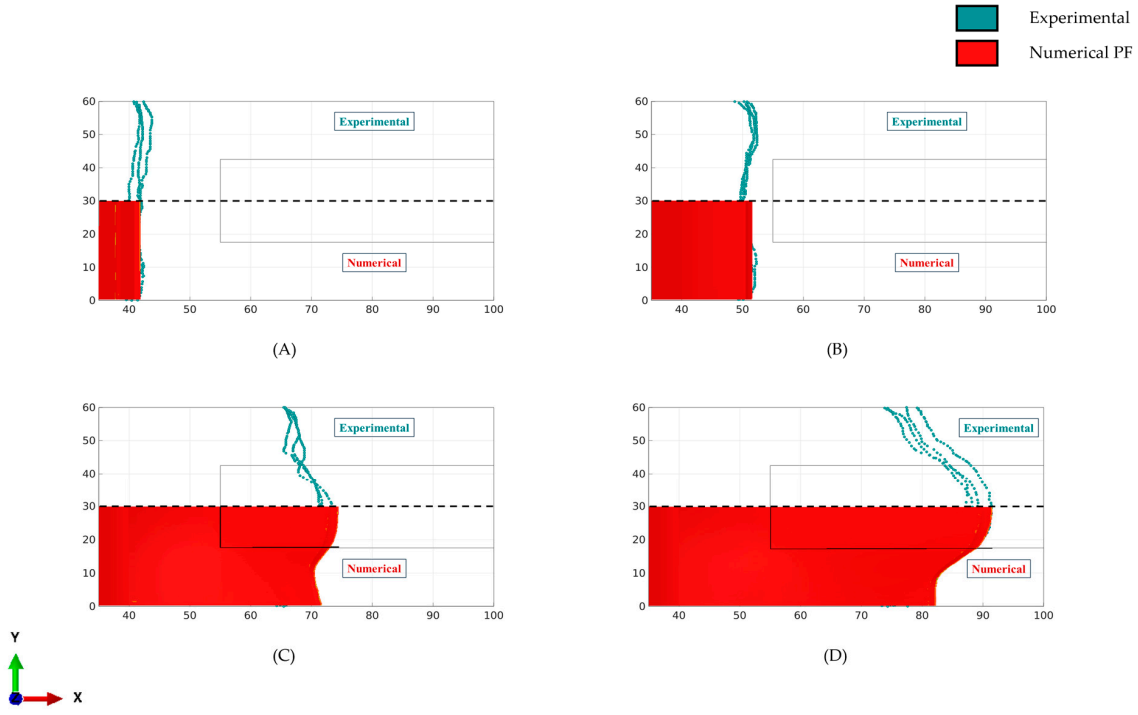

Figure 8. Comparison of the delamination front under Mode I loading conditions during repeated loading and unloading steps at displacements of (**A**) 4 mm, (**B**) 6 mm, (**C**) 12 mm, and (**D**) 15 mm. Experimental results from [87] were reproduced with permission from Elsevier.

Secondly, for the case of mode II-dominated failure, the ENF specimen consisted of two UD laminae stacked with an adhesive layer, designated as $[0^\circ_8//0^\circ_8]$. Figure 9A displays the dimensions of the sample. Each of the plates, labeled $[0^\circ_8]$, measures 100 mm in length and 1.47 mm in thickness, with an interface featuring an initial crack that extends 32 mm from one end. In the FE model, the part was represented by 176,800 hexahedral C3D8T elements with linear geometric order. Roller supports measuring 10 mm and 4 mm in diameter were modeled as rigid bodies using quadrilateral R3D4 elements, also with linear geometric order. The displacement was applied to the 10 mm roller, while the displacement of the lower rollers was fixed. Additionally, constraints were imposed on three nodes to prevent rigid body movement of the specimen. Lastly, the interaction between the rollers and the specimen was considered under the assumption that there was no friction. The properties for the CFRP and interface were consistent with those used in the previous case. The PF numerical analysis predicted a peak load of 531.71 N with a 7.49% error, with failure occurring at a displacement of 3.81 mm, which correlated well with the experimental envelope from the previous study [88], as illustrated in Figure 9B,C. The total CPU execution time for the staggered scheme was approximately 3.15 h for the DCB test case and 1.91 h for the ENF test case.

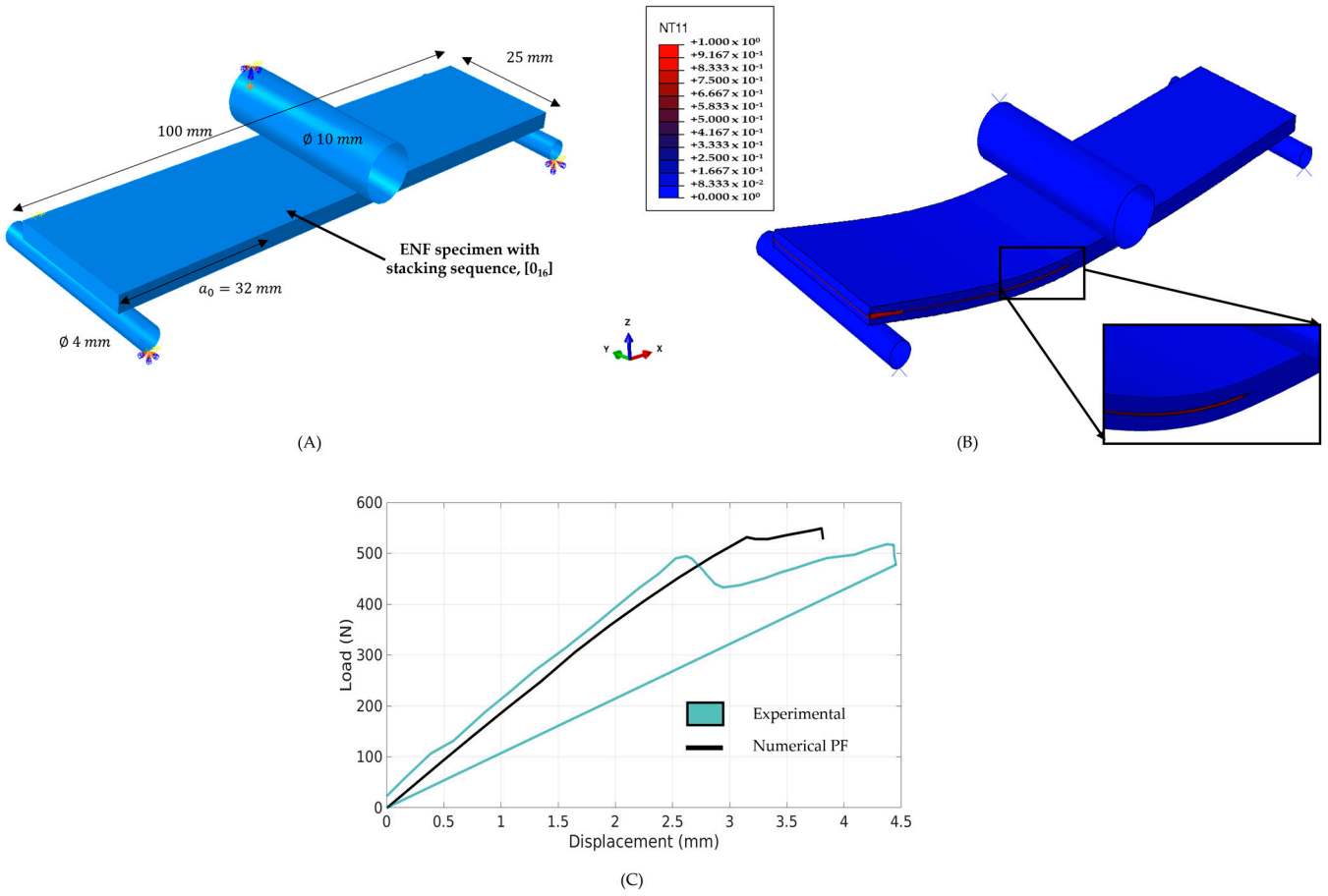

Figure 9. (**A**) Geometry and boundary conditions for the Mode II test, (**B**) evolution of damage along the interface with a scaling factor of 5.0, and (**C**) comparison of the load-displacement plot between experimental data [88] and the PF numerical model.

3.3. Coupled Computational Model for L-Shaped Composites

Upon completing the benchmark cases for pure mode I and mode II failures, we advanced to the more complex scenario of L-shaped laminate specimens. This test case simulated a bending-opening condition, which is characteristic of mixed-mode failure [30]. The coupons used in this study were fabricated using the hand layup method and cured in

an autoclave following the two-dwell MRCC process [78]. The MRCC process involved an initial temperature increase of 2 °C per minute up to 120 °C, followed by an isothermal hold for 60 min. A second temperature increase, at the same rate, raised the temperature to 180 °C, which was then held isothermally for 120 min. Finally, the temperature was gradually reduced to room temperature at a rate of 2 °C per minute. Similar to the benchmark case, a constant pressure of 7 bars was applied throughout the process. After manufacturing, the test setup was designed to apply a combination of moment and axial loading to the specimens. Each specimen was mounted on a freely rotating pin within the loading fixture, which was secured to a hydraulic 250 kN static testing machine. The load was applied vertically, and the specimen was loaded at a rate of 1 mm/min. The angle between the arms and the inner radius at the bend section was 90°, with an inner radius of 8 mm. The laminate thicknesses for the thin and thick layers were 3.31 mm and 5.52 mm, respectively, following the stacking sequences of $[0°_3//90°_3//0°_3]$ s and $[0°_3//90°_3//0°_3//90°_3//0°_3]$ s. Prior to testing, the specimen surfaces were polished, painted white, and coated with speckle patterns to aid in the observation of inter- and intralaminar crack propagation. In the FE model, the thin and thick sections were represented by 203,500 and 682,440 hexahedral elements, respectively, each with linear geometric order and allocated local orientations. The mold, which was assumed to have a negligible CTE, was modeled as a rigid component using 10,730 quadrilateral R3D4 elements. The boundary conditions for the thin sample case are shown in Figure 10A.

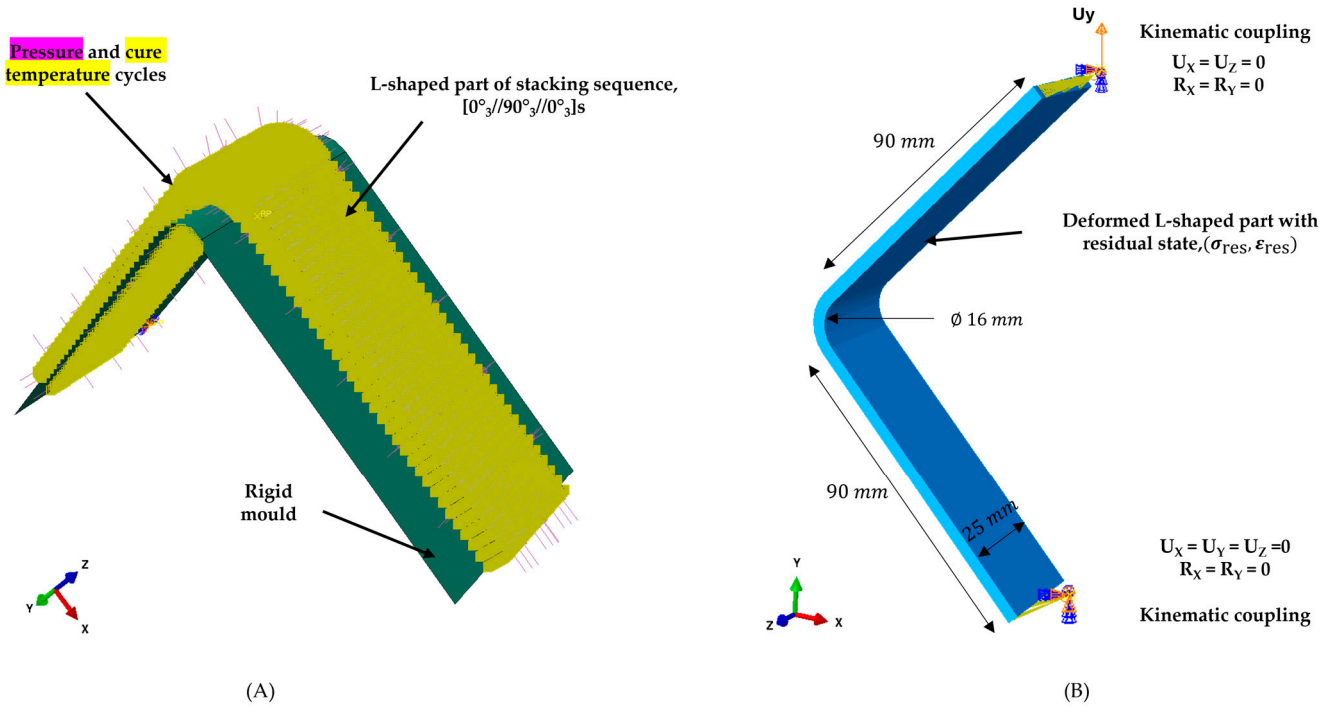

Figure 10. Associated boundary conditions for (**A**) the curing simulation using the CHILE model and (**B**) the structural simulation using the PF model, respectively.

For the case of the thin sample, the spring-in effect observed during the demolding step with the CHILE model resulted in induced deformations and a residual stress field, as illustrated in Figure 11. The shear components were observed to be minimal compared to those in the primary directions. Notably, the tensile residual stresses within the 90° plies were near the material's tensile strength, at approximately 64 MPa. Additionally, through-thickness residual stresses were significantly higher in the inner 0° plies compared to the 90° plies. The residual state post-demolding is critical, as these stresses persist after manufacturing and may impact the in-service strength of the thermoset part.

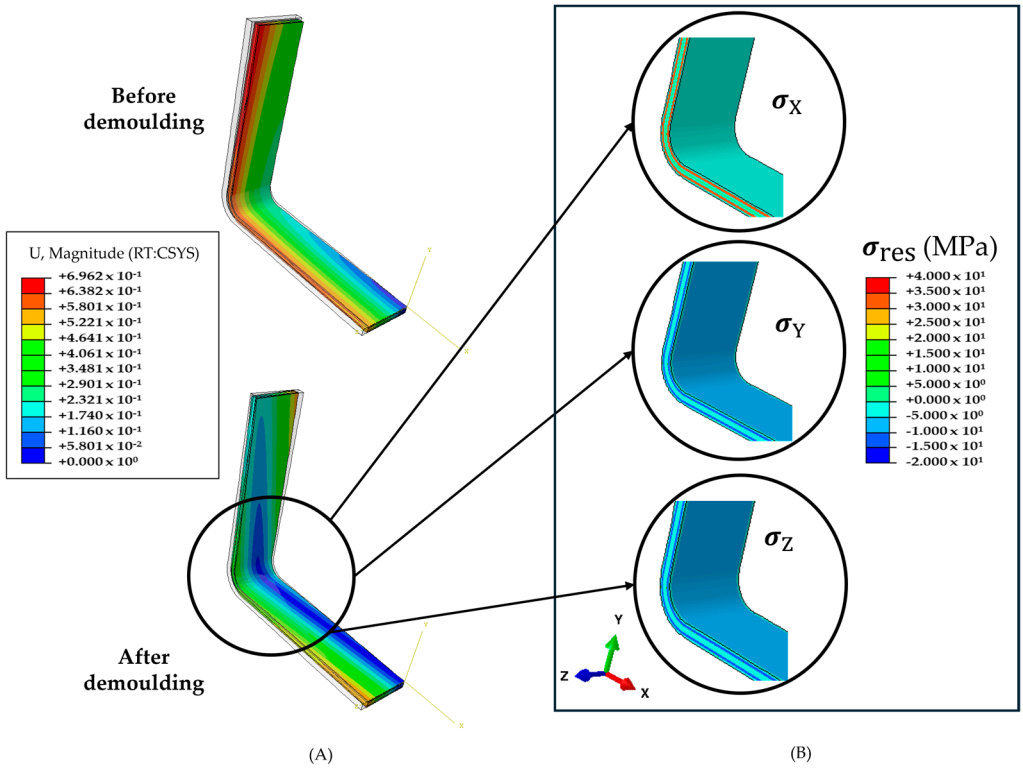

Figure 11. (**A**) The overall deformation before and after the demolding step in the curing simulation with respect to the affixed CSYS, and (**B**) the associated residual stress upon demolding in the primary global directions (with a deformation scaling factor of 1.0).

After the demolding step, the cured L-shaped part was subjected to a bending-opening load configuration, consistent with the experiment, as depicted in Figure 10B. In the FE model, the boundary conditions were idealized using kinematic coupling, which connected the load to the specimen's edge surfaces through reference points [36]. This configuration allowed for displacement along the Y-axis at the top load point and permitted rotation around the Z-axis at the top and bottom load points, effectively simulating a free rotation. The rest of the degrees of freedom were constrained at both points.

The failure mechanisms in the curved section of the thin sample under loading included interlaminar delamination and matrix-induced cracking. Figures 12 and 13 present the inter- and intralaminar crack regions denoted by $\phi > 0.97$, along with the load-displacement plots comparing experimental and numerical results. The experiments revealed a spread in the measured maximum load drops. The load drop corresponded to delamination across the curved section, followed by a slow and steady propagation of failure into the arms. The PF analysis that included residual stress closely aligned with the experimental envelope, highlighting the importance of considering the locked-in residual stresses within the part. This is because tensile residual stresses make matrix-induced cracking in the 90° layers more noticeable. As a result, the load level decreased from 441 N to 408 N when accounting for these residual stresses, compared to the case without residual stresses.

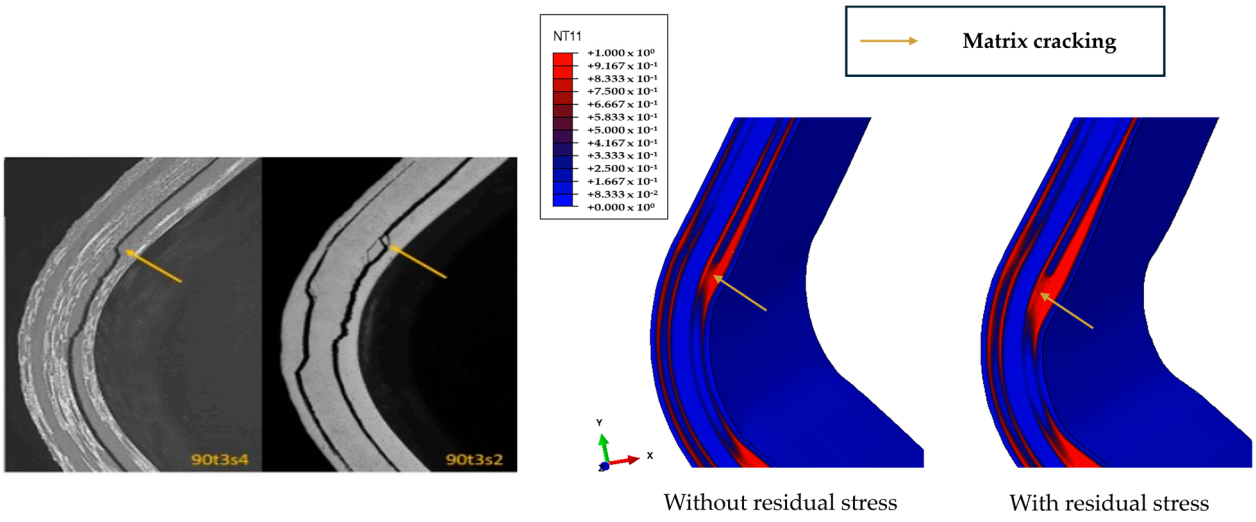

Figure 12. Comparison of delamination and matrix cracking in 90° plies based on (**A**) experimental data [30] and (**B**) numerical PF simulations. Experimental results from ref. [30] were reproduced with permission from Elsevier.

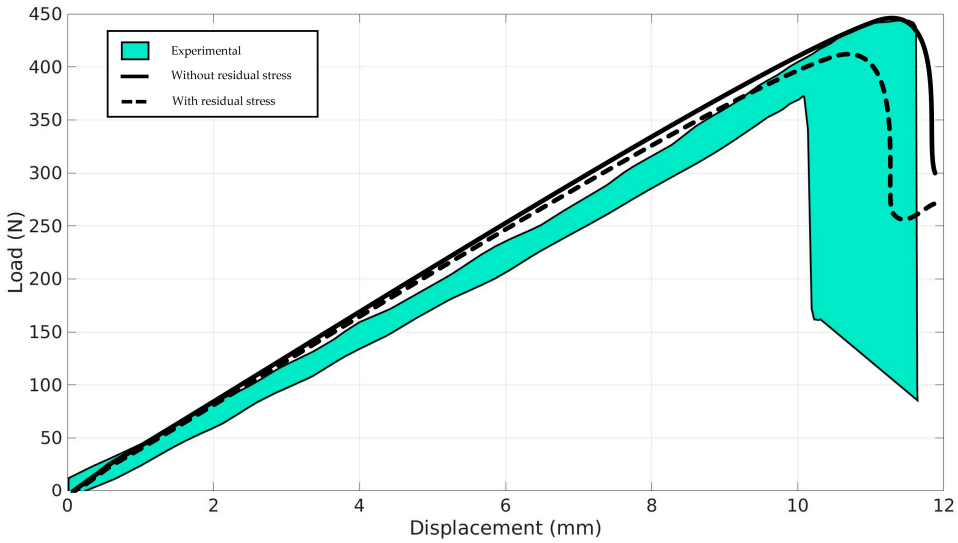

Figure 13. Comparison of failure loads based on experimental data [30] and numerical PF simulations, with and without manufacturing-induced residual stresses.

The total CPU time incurred with the coupled approach was approximately 4.94 h. The proposed coupled computational approach provides an initial estimation of the impact of cure-induced residual stresses and serves to optimize cure temperature profiles. Two common strategies for modifying the MRCC without requiring additional post-cure cycles are (a) 100 modified stochastic cooling rates between 0.5–2.0 °C/min and (b) 100 three-dwell cure cycles, introducing an additional isothermal zone between 120 °C and 180 °C. In the second and third dwell cycles, stochastic heating rates range from 0.5–2.0 °C/min, while the intermediate isothermal dwell lasts between 60–100 min. These modified zones are illustrated in Figure 14A. A stochastic coupled computational approach was applied to various cases, and the nodal values of the ϕ, corresponding to the 90° plies, were post-processed. A comparison of the nodal values between different models was implemented using the failure probability metric. The failure probability was defined as the ratio of the

number of nodes with $\phi > 0.97$ (indicating failure) to the total number of nodes in the 90° plies.

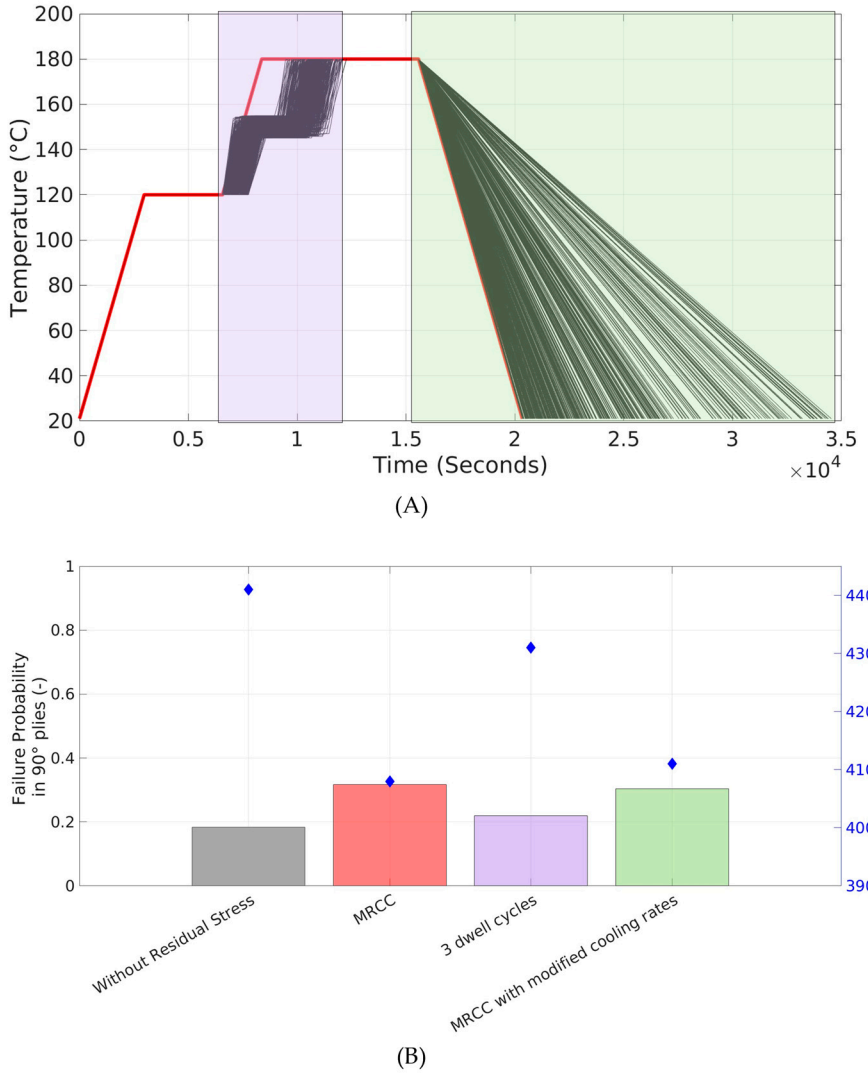

Figure 14. (**A**) MRCC (indicated by the red line) and various stochastic thermal loading conditions corresponding to three-dwell cure cycles and modified slower cooling rates; and (**B**) comparison of failure probabilities in 90° plies under different thermal loading conditions, along with the peak load before failure.

The comparison of failure probabilities within the 90° plies is depicted in Figure 14B. It is noted that while the slower cooling rate strategy results in a 6.45% reduction in failure probability, the three-dwell cure cycle approach yields a significant reduction of 32.26%. This improvement is attributed to the introduction of the third isothermal dwell, which delays the transition between the rubbery and glassy states. Consequently, this approach locks in a relatively lower residual stress state associated with higher modulus values in the glassy state. Meanwhile, lower cooling rates promote a more uniform temperature distribution throughout the material, thereby reducing internal stresses. Post-processing results indicated that the average tensile residual stresses for the modified three-dwell cycles and modified cooling rates were 31 MPa and 41 MPa, respectively. Furthermore, the peak load at failure was observed to have improved by 5.64% and 0.94% compared to the MRCC. Similar to the conclusions drawn in the previous study [89], it is emphasized that adjusting the cure conditions concerning the cooling zone is less feasible in terms of production costs compared to adding an extra isothermal dwell within the cure cycle.

The coupled numerical approach was then applied to the thick specimen. The failure pattern predicted by the PF numerical analysis closely correlates with the experimental observations, as shown in Figure 15. Furthermore, the shift in delamination between the interfaces associated with the 90° plies, especially around the inner radius of the specimen where matrix cracking occurs, is accurately replicated.

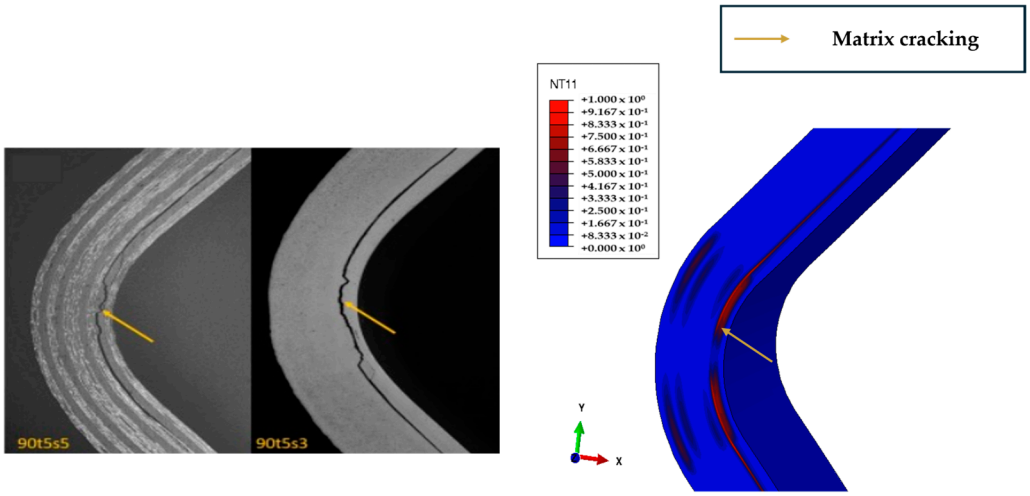

Figure 15. Comparison of delamination and matrix cracking in 90° plies for a thick L-shaped specimen based on (**A**) experimental data [30] and (**B**) numerical PF simulations without residual stress. Experimental results from ref. [30] were reproduced with permission from Elsevier.

However, it is essential to recognize the presence of random process-induced voids within the 90° plies, as illustrated in Figure 16A. The existence of these stochastic voids should be taken into account during both the cure and structural numerical analyses. Random voids, represented as gaussian random non-zero nodes, were generated over the 3D mesh of the L-shaped part. A comprehensive explanation of this approach is available in a previous study [90]. The randomly generated non-zero nodes were established based on the void percentage, which is a function of the applied pressure in the cure boundary condition, as described in [91]. This relationship is illustrated in Figure 16B. These correlations were utilized to examine and compare the localization of the residual stress fields in the thick L-shaped part. Figure 16C displays one of the random stochastic configurations corresponding to void ratios of 0.5%, 2.0%, and 3.0%, respectively. The randomly generated voids were not assigned thermo-chemo-mechanical properties and damage phase values (ϕ = 0.97) in the curing and structural numerical analyses, respectively, to accurately replicate the effects of voids within the numerical model. The cure numerical analysis reveals that as the void ratios increased, there was a significant localization of the residual stress fields. Residual stress associated with edge delamination was present in all three cases; however, as the void ratio increased, we observed the formation of localized stress fields in the primary directions at the curved section. Therefore, it is essential to understand how this localization influences the peak failure loads in subsequent structural analyses.

The localized stress field initialized within the PF framework influenced the peak failure loads in the load-displacement plots. Figure 17 illustrates the mean load-displacement responses for the three cases involving 100 stochastic voids, alongside the case without residual stress. Notably, the stochastic PF analysis with a 0.5% void ratio shows a closer correlation with the experiments, achieving a peak load of 829 N compared to 889 N for the case without voids. Meanwhile, the peak load decreases by 14.23% and 20.74% when the void ratio is increased from 0.5% to 2.0% and 3.0%, respectively. This illustrates that the increasing void percentage and the corresponding rise in localized residual stress adversely impact matrix cracking in the thick parts. It is important to note that the assumption of no

covariance between the void ratio and fracture properties has been made and should be revisited in future.

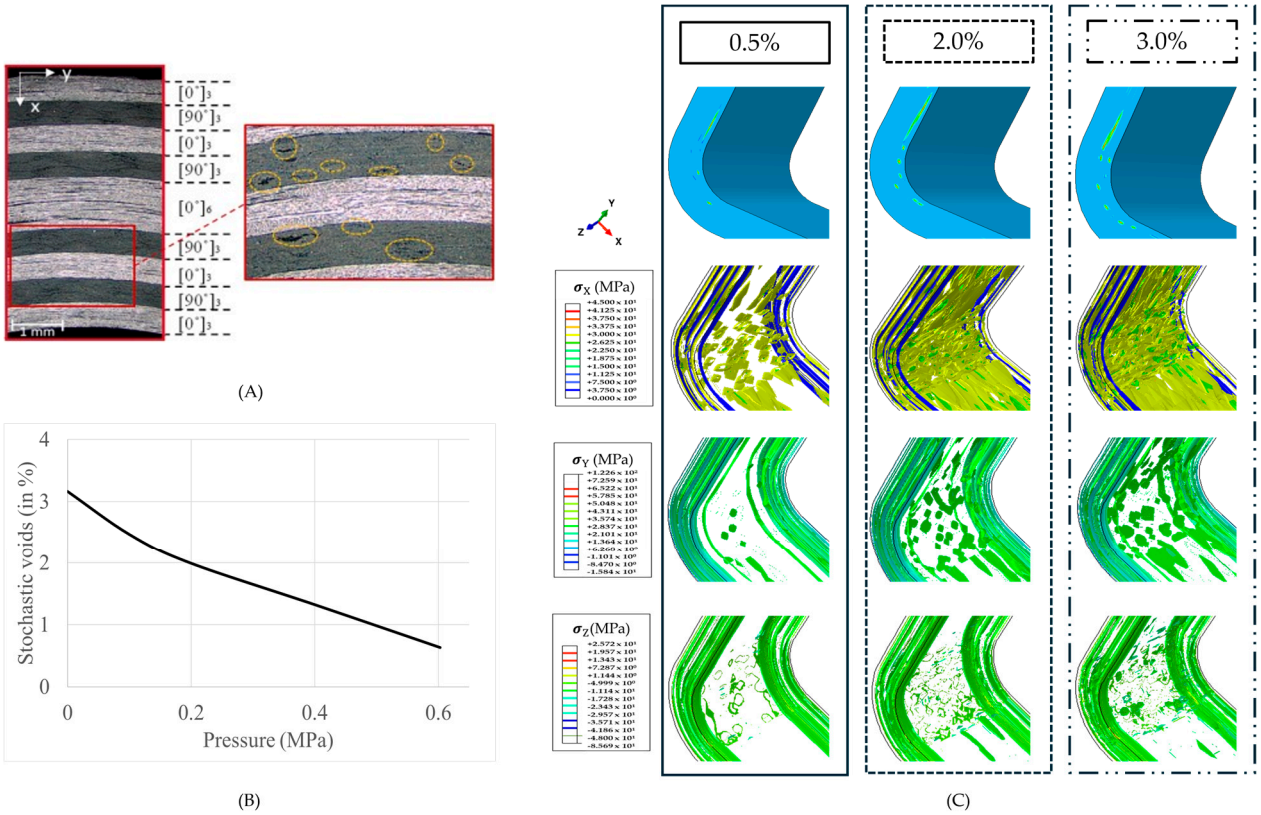

Figure 16. (**A**) Voids in 90° plies within the thick specimen (experimental image from ref. [30] was reproduced with permission from Elsevier), (**B**) correlation between curing pressure conditions and void ratio [91], and (**C**) schematic representation of random voids along with localized residual stress concentration corresponding to 0.5%, 2.5%, and 3.5% void contents, respectively.

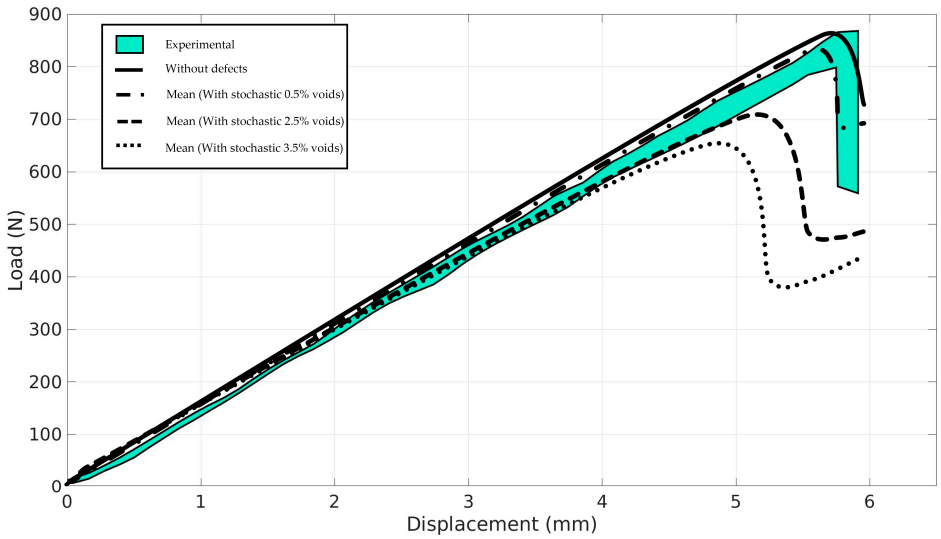

Figure 17. Comparison of the mean load-displacement plots for stochastic voids within the 90° plies, corresponding to 0.5%, 2.5%, and 3.5% void content alongside experimental data [30], respectively.

4. Conclusions

Manufacturing defects are an unavoidable aspect of producing composite parts. Consequently, it is crucial to comprehend how these defects influence the structural response of manufactured composite components. This study focused on examining the influence of "locked-in" internal residual stress fields on the load-carrying capacity and strength of composite parts, particularly those with curvatures commonly used in aerospace applications. The nature and magnitude of these stress fields are significantly influenced by the curing thermal loading conditions, which dictate the evolution of cure state variables and, in turn, inform the development of thermal, chemical, and mechanical properties at the meso-level of the homogeneous lamina. For the numerical case study, coupled computational models—comprising the CHILE model and the PF model—were applied to an L-shaped composite part with varying thicknesses and cross-ply configurations, involving AS4/8552 prepregs.

When cure loading conditions involve the MRCC, internal residual stresses are crucial, especially tensile residual stresses in the hoop direction of the curved sections of thermoset composite components. The magnitude of these localized stress fields approaches the tensile strength of the lamina. When subjected to mechanical loading in scenarios such as bending-opening with mixed-mode effects, there is significantly more damage related to intralaminar matrix cracking compared to cases without cure-induced residual stresses. The presence of increased bulk matrix cracking results in a premature loss of load-carrying capacity, aligning well with the experiments. This coupled approach facilitates the optimization of cure thermal loading profiles, thereby reducing risks and improving the manufacturing quality by accounting for the curing phenomenon. This study explored various stochastic cure-coupled PF simulations that incorporated three-dwell cure cycles and cooling conditions. The three-dwell cure cycle emerged as the most effective solution, as it deliberately delays the transition between rubbery and glassy states during curing. This delay, in turn, leads to reduced bulk matrix cracking under structural loads.

Furthermore, the analysis of thick L-shaped parts took into account the presence of varying stochastic void content, as these voids induce localized internal residual stresses during manufacturing. The effects of such localized stresses, when incorporated into the PF model, were analyzed under similar loading conditions. In the future, it will be crucial to establish a clear correlation between voids and fracture or mechanical properties to improve the prediction accuracy. The proposed computational approach has significant potential for developing virtual manufacturing processes that incorporate new resin formulations in the industry. However, it is crucial to consider the specific chemical and physical properties of these formulations to ensure their accurate and effective implementation. Moreover, the coupled approach could be adapted for real-time monitoring by using an offline surrogate model trained on high-fidelity outputs, such as failure loads, displacement, and probability of failure, with loading conditions as inputs. Additionally, integrating intermediate machining processes—linking manufacturing stages to structural responses—can be a valuable aspect of future numerical analyses. A key limitation is the difficulty of implementing a transition area between plies with higher fiber volume fractions. While CZM-based interfacial cracks with PF models offer an alternative, challenges arise in calibrating the CHILE model parameters during curing. Additionally, applying the coupled approach to large-scale structures is challenging due to the need for a better understanding of PF model parameters in complex, multiscale structures. Despite these limitations, the approach holds promise for delivering comprehensive and reliable design evaluations in virtual manufacturing practices.

Author Contributions: Conceptualization, A.B., D.D. and O.P.; methodology, A.B.; software, A.B.; validation, A.B.; formal analysis, A.B.; investigation, A.B.; resources, A.B.; data curation, A.B.; writing—original draft preparation, A.B.; writing—review and editing, D.D.; visualization, A.B., D.D., and O.P.; supervision, D.D. and O.P.; project administration, D.D.; funding acquisition, D.D. All authors have read and agreed to the published version of the manuscript.

Funding: This project has received funding from the European Union's Horizon 2020 research and innovation program under the Marie Skłodowska-Curie grant agreement no. 859957.

Data Availability Statement: Data sharing is not applicable to this article as no datasets were generated during the current study.

Acknowledgments: The present research benefited from computational resources made available on Lucia, the Tier-1 supercomputer of the Walloon Region, infrastructure funded by the Walloon Region under grant agreement no. 1910247. Portions of this work were completed while one author (Olivier Pierard) was affiliated with Cenaero Research Center.

Conflicts of Interest: The authors declare no conflicts of interest.

Appendix A. Cure State Variables and Volumetric Free Strains

The key variables relevant to the cure process include the degree of cure, ϱ, the glass transition temperature, T_g, volumetric free strains, CTEs and CCSs, the gel point (ϱ_{gel}), the vitrification point (ϱ_{vitr}) and the mechanical properties at different states. The variable ϱ is the ratio between the heat released at initial time and the total amount of heat released during the curing process. This ratio ranges from 0 to 1, and it serves as a state variable for estimation. The degree of cure describes the system's state during curing, representing the ratio of heat released at a specific time to the total heat released throughout the process. As the material approaches the glassy state, molecular mobility decreases significantly due to the reduction in resin volume. This transition is defined by the glass transition temperature, T_g.

After the vitrification stage, molecular mobility significantly decreases due to the reduction in resin volume, emphasizing the need to control the cure rate. The transformation from the rubbery to the glassy state occurs when the cure temperature, T, matches with T_g, which is known to depend on ϱ. This relationship is described by DiBenedetto's relationship [92]. A cure kinetics model that incorporates diffusion control to capture this phenomenon is applied [79]. Furthermore, the material properties are anisotropic and vary at different stages of curing. The volumetric free strain, $\boldsymbol{\varepsilon}$, is associated to the state variables, given by

$$\boldsymbol{\varepsilon} = \boldsymbol{\varepsilon}^{\text{th}} + \boldsymbol{\varepsilon}^{ch} \tag{A1}$$

$$\boldsymbol{\varepsilon}^{\text{th}} = \int_0^t \alpha(\varrho, T)\left(\frac{\partial T}{\partial t}\right)dt \text{ and } \boldsymbol{\varepsilon}^{ch} = \int_0^t \beta(\varrho, T)\left(\frac{\partial \varrho}{\partial t}\right)dt$$
$$\text{with } \alpha \mid \beta = \begin{cases} \alpha^v \mid \beta^v \ \forall\, \varrho < \varrho_{\text{gel}} \text{ and } T \geq T_g \\ \alpha^r \mid \beta^r \ \forall\, \varrho \geq \varrho_{\text{gel}} \text{ and } T \geq T_g \\ \alpha^g \mid \beta^g \ \forall\ T < T_g \end{cases} \tag{A2}$$

where α^i and β^i represent the CTEs and CCSs in various states throughout the cure process, respectively. Expansion strains are regarded as negligible in the viscous state. When transitioning to the rubbery state, there is a decrease in the free volume due to chemical shrinkage, coupled with matrix expansion resulting from thermal effects. Additionally, entering the glassy state marks the completion of the cross-linking reaction, i.e., the influence of chemical shrinkage becomes less significant. It is important to note that thermal effects are not considered when the isothermal temperature remains stable, but they are relevant during the cooling phase of the curing cycle.

Appendix B. Approximation of Diffuse Crack Topology

An example of a 1D bar loaded at both ends is used to illustrate the PF approximation of diffuse crack topology. Assuming that damage initiates with cracks, an exponential function corresponding to the AT2 model is defined to represent the non-smooth crack topology, expressed as follows:

$$\phi(x) = e^{\frac{-|x|}{l_\phi}} \tag{A3}$$

where ϕ represents the damage, $\phi(0) = 1$ indicates the completely damaged state and $\phi(\pm\infty) = 0$ represents the undamaged state. It represents the solution to the homogeneous differential equation [40] given by $\phi(x) - {l_\phi}^2\phi''(x) = 0$ in Ω subject to the Dirichlet condition. The variational principle in its strong form, as expressed in Equation (A3) [40], is given as follows:

$$\phi = \text{Arg}\left\{\inf_{\phi \in H_c} \Gamma_\phi\right\} \tag{A4}$$

where $H_c = \{\phi | \phi(0) = 1 \text{ and } \phi | \phi(\pm\infty) = 0\}$. The crack surface functional, denoted as $\Gamma_\phi = \int \gamma(\phi, \nabla\phi) d\Omega$, represents the crack surface area. Here, γ is the surface density functional, and when extended to 3D problems, it is expressed in general form as

$$\gamma(\phi, \nabla\phi) = \frac{1}{2}\left(\frac{\phi^2}{l_\phi} + l_\phi . ||\nabla\phi||^2\right) \tag{A5}$$

Appendix C. Material Parameters for the Helmholtz Free Energy Function

According to [71], for transversely isotropic UD composites, the material parameters $o_{i=1,2...5}$ in the Helmholtz free energy function are defined by

$$o_1 = y_2; o_2 = \frac{y_1}{2};\ \ o_3 = y_3;\ o_4 = \frac{y_4}{2} + o_2; o_5 = y_5 \tag{A6}$$

The parameters $y_{i=1,2...5}$ are related to the mechanical properties that define the linear elastic Hooke tensor, $\boldsymbol{C}$, assuming an axis of isotropy is given by

$$\begin{gathered} y_1 = C_{11} - C_{12};\ \ y_2 = C_{12};\ y_3 = C_{13} - C_{12} \\ y_4 = 2(C_{55} - C_{66}); y_5 = C_{11} + C_{33} - 2C_{13} - 4C_{55} \end{gathered} \tag{A7}$$

This corresponds to the case of UD transverse isotropy, where $C_{11} = C_{22}$, $C_{23} = C_{31}$, $C_{44} = C_{55}$, and $C_{66} = (C_{11} - C_{12})/2$.

References

1. Neveu, F.; Castanié, B.; Olivier, P. The GAP methodology: A new way to design composite structures. *Mater. Des.* **2019**, *172*, 107755. [CrossRef]
2. Advani, S.G.; Sozer, E. *Process Modeling in Composites Manufacturing*, 2nd ed.; CRC Press: Boca Raton, FL, USA, 2010.
3. Talreja, R. Manufacturing defects in composites and their effects on performance. In *Polymer Composites in the Aerospace Industry*; Irving, P.E., Soutis, C., Eds.; Woodhead Publishing: Cambridge, UK, 2015; pp. 99–113.
4. Senthil, K.; Arockiarajan, A.; Palaninathan, R.; Santhosh, B.; Usha, K.M. Defects in composite structures: Its effects and prediction methods—A comprehensive review. *Compos. Struct.* **2013**, *106*, 139–149. [CrossRef]
5. Zobeiry, N.; Poursartip, A. The origins of residual stress and its evaluation in composite materials. In *Structural Integrity and Durability of Advanced Composites*; Beaumont, P.W.R., Soutis, C., Hodzic, A., Eds.; Woodhead Publishing: Cambridge, UK, 2015; pp. 43–72.
6. Agius, S.L.; Joosten, M.; Trippit, B.; Wang, C.H.; Hilditch, T. Rapidly cured epoxy/anhydride composites: Effect of residual stress on laminate shear strength. *Compos. A Appl. Sci. Manufact.* **2016**, *90*, 125–136. [CrossRef]
7. Joosten, M.W.; Agius, S.; Hilditch, T.; Wang, C. Effect of residual stress on the matrix fatigue cracking of rapidly cured epoxy/anhydride composites. *Compos. A Appl. Sci. Manufact.* **2017**, *101*, 521–528. [CrossRef]
8. Zhao, L.G.; Warrior, N.A.; Long, A.C. A micromechanical study of residual stress and its effect on transverse failure in polymer–matrix composites. *Int. J. Solids Struct.* **2006**, *43*, 5449–5467. [CrossRef]
9. Garstka, T.; Ersoy, N.; Potter, K.D.; Wisnom, M.R. In situ measurements of through-the-thickness strains during processing of AS4/8552 composite. *Compos. A Appl. Sci. Manufact.* **2007**, *38*, 2517–2526. [CrossRef]
10. Lahtinen, H. Calculation of residual stresses of cross-ply laminates. *J. Compos. Mater.* **2003**, *37*, 945–966. [CrossRef]
11. Shokrieh, M.M.; Ghanei Mohammadi, A.R. The importance of measuring residual stresses in composite materials. In *Residual Stresses in Composite Materials*; Shokrieh, M.M., Ed.; Woodhead Publishing: Cambridge, UK, 2014; pp. 3–14.
12. Radford, D.W.; Rennick, T.S. Separating sources of manufacturing distortion in laminated composites. *J. Reinf. Plast. Compos.* **2000**, *19*, 621–641. [CrossRef]
13. Ersoy, N.; Potter, K.; Wisnom, M.R.; Clegg, M.J. Development of spring-in angle during cure of a thermosetting composite. *Compos. A Appl. Sci. Manufact.* **2005**, *36*, 1700–1706. [CrossRef]

14. Seers, B.; Tomlinson, R.; Fairclough, P. Residual stress in fiber reinforced thermosetting composites: A review of measurement techniques. *Polym. Compos.* **2021**, *42*, 1631–1647. [CrossRef]
15. Ghasemi, A.R.; Mohammadi-Fesharaki, M. Influence of different parameters on cured shapes and residual stresses of unsymmetric composite laminate reinforced by multi-wall carbon nanotubes. *Polym. Bull.* **2019**, *76*, 5751–5771. [CrossRef]
16. Twigg, G.; Poursartip, A.; Fernlund, G. Tool–part interaction in composites processing. Part I: Experimental investigation and analytical model. *Compos. A Appl. Sci. Manufact.* **2004**, *35*, 121–133. [CrossRef]
17. Parmentier, A.; Dumas, D. Influence of the tool-part frictional interaction on the cure-induced deformations in thermoset-based composite parts. In Proceedings of the 21st International Conference on Composite Materials, Xi'an, China, 20–25 August 2017.
18. Wang, B.; Fan, S.; Chen, J.; Yang, W.; Liu, W.; Li, Y. A review on prediction and control of curing process-induced deformation of continuous fiber-reinforced thermosetting composite structures. *Compos. A Appl. Sci. Manufact.* **2023**, *165*, 107321. [CrossRef]
19. Ding, A.; Li, S.; Sun, J.; Wang, J.; Zu, L. A comparison of process-induced residual stresses and distortions in composite structures with different constitutive laws. *J. Reinf. Plast. Compos.* **2016**, *35*, 807–823. [CrossRef]
20. White, S.R.; Hahn, H.T. Process modeling of composite materials: Residual stress development during cure. Part II. Experimental validation. *J. Compos. Mater.* **1992**, *26*, 2423–2453. [CrossRef]
21. Kim, Y.R.; White, S.R. Viscoelastic analysis of processing-induced residual stresses in thick composite laminates. *Mech. Compos. Mater. Struct.* **1997**, *4*, 361–387. [CrossRef]
22. Prasatya, P.; McKenna, G.B.; Simon, S.L. A viscoelastic model for predicting isotropic residual stresses in thermosetting materials: Effects of processing parameters. *J. Compos. Mater.* **2001**, *35*, 826–848. [CrossRef]
23. Ding, A.; Li, S.; Wang, J.; Zu, L. A three-dimensional thermo-viscoelastic analysis of process-induced residual stress in composite laminates. *Compos. Struct.* **2015**, *129*, 60–69. [CrossRef]
24. Johnston, A.A.; Vaziri, R.; Poursartip, A. A plane strain model for process-induced deformation of laminated composite structures. *J. Compos. Mater.* **2001**, *35*, 1435–1469. [CrossRef]
25. Svanberg, J.M.; Holmberg, J.A. Prediction of shape distortions. Part I: FE-implementation of a path dependent constitutive model. *Compos. A Appl. Sci. Manufact.* **2004**, *35*, 711–721. [CrossRef]
26. Zobeiry, N.; Vaziri, R.; Poursartip, A. Computationally efficient pseudo-viscoelastic models for evaluation of residual stresses in thermoset polymer composites during cure. *Compos. A Appl. Sci. Manufact.* **2010**, *41*, 247–256. [CrossRef]
27. Gözlüklü, B.; Coker, D. Modeling of the dynamic delamination of L-shaped unidirectional laminated composites. *Compos. Struct.* **2012**, *94*, 1430–1442. [CrossRef]
28. Geleta, T.N.; Woo, K.; Lee, B. Delamination behavior of L-shaped laminated composites. *Int. J. Aeronaut. Space Sci.* **2018**, *19*, 363–374. [CrossRef]
29. Cao, D.; Hu, H.; Duan, Q.; Song, P.; Li, S. Experimental and three-dimensional numerical investigation of matrix cracking and delamination interaction with edge effect of curved composite laminates. *Compos. Struct.* **2019**, *225*, 111154. [CrossRef]
30. Tasdemir, B.; Coker, D. Comparison of damage mechanisms in curved composite laminates under static and fatigue loading. *Compos. Struct.* **2019**, *213*, 190–203. [CrossRef]
31. Martin, R.H.; Jackson, W.C. *Damage Prediction In Cross-Plied Curved Composite Laminates*; NASA Technical Memorandum 104089, AVSCOM-TR-91-B-009; NASA Langley Research Center: Hampton, VA, USA, 1991. Available online: https://ntrs.nasa.gov/citations/19910021253 (accessed on 12th August 2022).
32. Cheng, Z.-Q.; Liu, H.; Tan, W. Advanced computational modelling of composite materials. *Eng. Fract. Mech.* **2024**, *305*, 110120. [CrossRef]
33. Cao, D.; Duan, Q.; Hu, H.; Zhong, Y.; Li, S. Computational investigation of both intra-laminar matrix cracking and inter-laminar delamination of curved composite components with cohesive elements. *Compos. Struct.* **2018**, *192*, 300–309. [CrossRef]
34. Andraju, L.B.; Raju, G. Continuum and cohesive zone damage models to study intra/inter-laminar failure of curved composite laminates under four-point bending. *Compos. Struct.* **2020**, *253*, 112768. [CrossRef]
35. Journoud, P.; Bouvet, C.; Castanié, B.; Laurin, F.; Ratsifandrihana, L. Experimental and numerical analysis of unfolding failure of L-shaped CFRP specimens. *Compos. Struct.* **2020**, *232*, 111563. [CrossRef]
36. Ata, T.T.; Coker, D. 2D and 3D simulations of dynamic delamination in curved unidirectional CFRP laminates subjected to moment/axial combined loading. *Compos. Struct.* **2021**, *268*, 113899. [CrossRef]
37. De Borst, R. Numerical aspects of cohesive-zone models. *Eng. Fract. Mech.* **2003**, *70*, 1743–1757. [CrossRef]
38. De Borst, R.; Chen, L. Phase-field modelling of cohesive interface failure. *Int. J. Numer. Methods Eng.* **2024**, *125*, e7412. [CrossRef]
39. van der Meer, F.P. Mesolevel modeling of failure in composite laminates: Constitutive, kinematic and algorithmic aspects. *Arch. Comput. Methods Eng.* **2012**, *19*, 381–425. [CrossRef]
40. Miehe, C.; Welschinger, F.; Hofacker, M. Thermodynamically consistent phase-field models of fracture: Variational principles and multi-field FE implementations. *Int. J. Numer. Methods Eng.* **2010**, *83*, 1273–1311. [CrossRef]
41. Griffith, A.A. VI. The phenomena of rupture and flow in solids. *Philos. Trans. R. Soc. Lond. A* **1921**, *221*, 163–198.
42. Irwin, G. *Onset of Fast Crack Propagation in High Strength Steel and Aluminum Alloys*; Naval Research Laboratory: Washington, DC, USA, 1956; pp. 289–305.
43. Bourdin, B.; Francfort, G.A.; Marigo, J.J. Numerical experiments in revisited brittle fracture. *J. Mech. Phys. Solids* **2000**, *48*, 797–826. [CrossRef]
44. Bourdin, B.; Francfort, G.A.; Marigo, J.J. The variational approach to fracture. *J. Elast.* **2008**, *91*, 5–148. [CrossRef]

45. Ambati, M.; Gerasimov, T.; De Lorenzis, L. A review on phase-field models of brittle fracture and a new fast hybrid formulation. *Comput. Mech.* **2015**, *55*, 383–405. [CrossRef]
46. Bui, T.Q.; Hu, X. A review of phase-field models, fundamentals and their applications to composite laminates. *Eng. Fract. Mech.* **2021**, *248*, 107705. [CrossRef]
47. Espadas-Escalante, J.J.; Isaksson, P. Mesoscale analysis of the transverse cracking kinetics in woven composite laminates using a phase-field fracture theory. *Eng. Fract. Mech.* **2019**, *216*, 106523. [CrossRef]
48. Espadas-Escalante, J.J.; van Dijk, N.P.; Isaksson, P. A phase-field model for strength and fracture analyses of fiber-reinforced composites. *Compos. Sci. Technol.* **2019**, *174*, 58–67. [CrossRef]
49. Zhang, P.; Hu, X.; Bui, T.Q.; Yao, W. Phase field modeling of fracture in fiber reinforced composite laminate. *Int. J. Mech. Sci.* **2019**, *161–162*, 105008. [CrossRef]
50. Hansen-Dörr, A.C.; de Borst, R.; Hennig, P.; Kästner, M. Phase-field modelling of interface failure in brittle materials. *Comput. Methods Appl. Mech. Eng.* **2019**, *346*, 25–42. [CrossRef]
51. Quintanas-Corominas, A.; Reinoso, J.; Casoni, E.; Turon, A.; Mayugo, J.A. A phase field approach to simulate intralaminar and translaminar fracture in long fiber composite materials. *Compos. Struct.* **2019**, *220*, 899–911. [CrossRef]
52. Zhang, P.; Feng, Y.; Bui, T.Q.; Hu, X.; Yao, W. Modelling distinct failure mechanisms in composite materials by a combined phase field method. *Compos. Struct.* **2020**, *232*, 111551. [CrossRef]
53. Quintanas-Corominas, A.; Turon, A.; Reinoso, J.; Casoni, E.; Paggi, M.; Mayuko, J.A. A phase field approach enhanced with a cohesive zone model for modeling delamination induced by matrix cracking. *Comput. Methods Appl. Mech. Eng.* **2020**, *358*, 112618. [CrossRef]
54. Mandal, T.K.; Nguyen, V.P.; Wu, J.-Y. A length scale insensitive anisotropic phase field fracture model for hyperelastic composites. *Int. J. Mech. Sci.* **2020**, *188*, 105941. [CrossRef]
55. Kumar, P.K.A.V.; Dean, A.; Reinoso, J.; Paggi, M. A multi phase-field-cohesive zone model for laminated composites: Application to delamination migration. *Compos. Struct.* **2021**, *276*, 114471. [CrossRef]
56. Pranavi, D.; Rajagopal, A.; Reddy, J.N. Interaction of anisotropic crack phase field with interface cohesive zone model for fiber reinforced composites. *Compos. Struct.* **2021**, *270*, 114038. [CrossRef]
57. Kumar, A.; Sain, T. Phase field-based cohesive zone approach to model delamination in fiber-reinforced polymer composites. *Compos. Struct.* **2024**, *329*, 117751. [CrossRef]
58. Kumar, A.; Sain, T. A 3D multi-phase-field model for orientation-dependent complex crack interaction in fiber-reinforced composite laminates. *Eng. Fract. Mech.* **2024**, *303*, 110097. [CrossRef]
59. Li, X.; Zhou, C.; Xing, C.; He, A.; Yu, J.; Wang, G. A phase-field fracture model for fatigue behavior in fiber-reinforced composites. *Int. J. Mech. Sci.* **2024**, *269*, 108989. [CrossRef]
60. Clayton, J.D.; Knap, J. Phase field modeling of directional fracture in anisotropic polycrystals. *Comput. Mater. Sci.* **2015**, *98*, 158–169. [CrossRef]
61. Teichtmeister, S.; Kienle, D.; Aldakheel, F.; Keip, M.-A. Phase field modeling of fracture in anisotropic brittle solids. *Int. J. Non-Linear Mech.* **2017**, *97*, 1–21. [CrossRef]
62. Mehdikhani, M.; Petrov, N.A.; Straumit, I.; Melro, A.R.; Lomov, S.V.; Gorbatikh, L. The effect of voids on matrix cracking in composite laminates as revealed by combined computations at the micro- and meso-scales. *Compos. Part A Appl. Sci. Manuf.* **2019**, *117*, 180–192. [CrossRef]
63. Woo, K.; Nega, B.F.; Cairns, D.S.; Lua, J. Delamination behavior of L-shaped composite beam with manufacturing defects. *J. Mech. Sci. Technol.* **2020**, *34*, 3709–3720. [CrossRef]
64. Cinar, K.; Guven, I.; Ersoy, N. Effect of residual stress on the bending response of L-shaped composite laminates. *Compos. Struct.* **2020**, *246*, 112425. [CrossRef]
65. Woo, K.; Nega, B.F.; Cairns, D.S.; Lua, J. Three-dimensional failure behaviour of L-shaped laminated composite with wrinkles and defects. *Adv. Compos. Mater.* **2022**, *32*, 368–399. [CrossRef]
66. Journoud, P.; Bouvet, C.; Castanié, B.; Ratsifandrihana, L. Experimental analysis of the effects of wrinkles in the radius of curvature of L-shaped carbon-epoxy specimens on unfolding failure. *Compos. Part A Appl. Sci. Manuf.* **2022**, *158*, 106975. [CrossRef]
67. Zocher, M.A.; Groves, S.E.; Allen, D.H. A three-dimensional finite element formulation for thermoviscoelastic orthotropic media. *Int. J. Numer. Methods Eng.* **1997**, *40*, 2267–2288. [CrossRef]
68. Francfort, G.A.; Marigo, J.J. Revisiting brittle fracture as an energy minimization problem. *J. Mech. Phys. Solids* **1998**, *46*, 1319–1342. [CrossRef]
69. Wu, J.Y. A unified phase-field theory for the mechanics of damage and quasi-brittle failure. *J. Mech. Phys. Solids* **2017**, *103*, 72–99. [CrossRef]
70. Wu, J.Y.; Nguyen, V.P. A length scale insensitive phase-field damage model for brittle fracture. *J. Mech. Phys. Solids* **2018**, *119*, 20–42. [CrossRef]
71. Lubarda, V.A.; Chen, M.C. On the elastic moduli and compliances of transversely isotropic and orthotropic materials. *J. Mech. Mater. Struct.* **2008**, *3*, 153–171. [CrossRef]
72. Amor, H.; Marigo, J.J.; Maurini, C. Regularized formulation of the variational brittle fracture with unilateral contact: Numerical experiments. *J. Mech. Phys. Solids* **2009**, *57*, 1209–1229. [CrossRef]

73. Yu, H.; Hao, L.; Shen, R.; Guo, L.; Shen, Z.; Li, Y. A phase field model with the mixed-mode driving force of power-law relation. *Eng. Fract. Mech.* **2022**, *264*, 108265. [CrossRef]
74. Cahill, L.M.A.; Natarajan, S.; Bordas, S.P.A.; O'Higgins, R.M.; McCarthy, C.T. An experimental/numerical investigation into the main driving force for crack propagation in uni-directional fibre-reinforced composite laminae. *Compos. Struct.* **2014**, *107*, 119–130. [CrossRef]
75. Navidtehrani, Y.; Betegón, C.; Martínez-Pañeda, E. A simple and robust Abaqus implementation of the phase field fracture method. *Appl. Eng. Sci.* **2021**, *6*, 100050. [CrossRef]
76. Navidtehrani, Y.; Betegón, C.; Martínez-Pañeda, E. A unified Abaqus implementation of the phase field fracture method using only a user material subroutine. *Materials* **2021**, *14*, 1913. [CrossRef]
77. Papazafeiropoulos, G.; Muñiz-Calvente, M.; Martínez-Pañeda, E. Abaqus2Matlab: A suitable tool for finite element post-processing. *Adv. Eng. Softw.* **2017**, *105*, 9–16. [CrossRef]
78. Hexply 8552 Product Data Sheet. Mid-Toughened, High Strength, Damage-Resistant, Structural Epoxy Matrix. Hexcel: Stamford, CT, USA, 2016. Available online: https://www.hexcel.com/ (accessed on 16 October 2021).
79. Cole, K.C.; Hechler, J.J.; Noel, D. A new approach to modeling the cure kinetics of epoxy/amine thermosetting resins. 2. Application to a typical system based on bis [4-(diglycidylamino)phenyl]methane and bis(4-aminophenyl) sulfone. *Macromolecules* **1991**, *24*, 3098–3110. [CrossRef]
80. Verhoosel, C.V.; de Borst, R. A phase-field model for cohesive fracture. *Int. J. Numer. Methods Eng.* **2013**, *96*, 43–62. [CrossRef]
81. Bogetti, T.A.; Gillespie, J.W. Process-induced stress and deformation in thick-section thermoset composite laminates. *J. Compos. Mater.* **1992**, *26*, 626–660. [CrossRef]
82. Ersoy, N.; Garstka, T.; Potter, K.; Wisnom, M.R.; Porter, D.; Clegg, M.; Stringer, G. Development of the properties of a carbon fiber reinforced thermosetting composite through cure. *Compos. Part A Appl. Sci. Manuf.* **2010**, *41*, 401–409. [CrossRef]
83. Balaji, A.; Sbarufatti, C.; Dumas, D.; Parmentier, A.; Pierard, O.; Cadini, F. Prediction of shape distortions in thermosetting composite parts using neural network interfaced visco-elastic constitutive model. *J. Compos. Mater.* **2024**, *58*, 1439–1459. [CrossRef]
84. Balaji, A.; Dumas, D.; Pierard, O.; Sbarufatti, C.; Cadini, F. Particle filter-based prognostics for composite curing process. *Polym. Compos.* **2024**, *45*, 12913–12931.
85. *ASTM Standard D5528*; Standard Test Method for Mode I Interlaminar Fracture Toughness of Unidirectional Fiber-Reinforced Polymer Matrix Composites. ASTM International: West Conshohocken, PA, USA, 2022.
86. *ASTM Standard D7905/D7905M*; Standard Test Method for Determination of the Mode II Interlaminar Fracture Toughness of Unidirectional Fiber-Reinforced Polymer Matrix Composites. ASTM International: West Conshohocken, PA, USA, 2019.
87. Carreras, T.; Renart, J.; Turon, A.; Costa, J.; Bak, B.L.V.; Lindgaard, E.; Martin de la Escalera, F.; Essa, Y. A benchmark test for validating 3D simulation methods for delamination growth under quasi-static and fatigue loading. *Compos. Struct.* **2019**, *210*, 932–941. [CrossRef]
88. Rajaneesh, A.; Bruyneel, M. Low-velocity impact and compression after impact modeling of composites using modified mesoscale model. *Compos. Struct.* **2023**, *311*, 116821.
89. Sicot, O.; Gong, X.L.; Cherouat, A.; Lu, J. Determination of residual stress in composite laminates using the incremental hole-drilling method. *J. Compos. Mater.* **2003**, *37*, 831–844. [CrossRef]
90. Zein, S.; Laurent, A.; Dumas, D. Simulation of a Gaussian Random Field over a 3-D Surface for the Uncertainty Quantification in the Composite Structures. *Comput. Mech.* **2019**, *63*, 1083–1090. [CrossRef]
91. Liu, L.; Zhang, B.-M.; Wang, D.-F.; Wu, Z.-J. Effects of cure cycles on void content and mechanical properties of composite laminates. *Compos. Struct.* **2006**, *73*, 303–309. [CrossRef]
92. Stutz, H.; Illers, K.H.; Mertes, J. A generalized theory for the glass transition temperature of crosslinked and un-crosslinked polymers. *J. Polym. Sci. Part B Polym. Phys.* **1990**, *28*, 1483–1498. [CrossRef]